nature communications

Article

https://doi.org/10.1038/s41467-025-57530-1

Parvimonas micra promotes oral squamous cell carcinoma metastasis through TmpC-CKAP4 axis

Received: 11 July 2024

Accepted: 25 February 2025

Published online: 07 March 2025

Check for updates

Houbao Qi[1,4], Haiting Gao[1,4], Meihui Li[1], Tianyong Sun[1], Xiufeng Gu[1], Li Wei[1], Mengfan Zhi[1], Zixuan Li[2], Dachuan Fu[1], Yiran Liu[3], Ziyi Wei[1], Yu Dou[1] & Qiang Feng[1]

Parvimonas micra (*P. micra*), an opportunistic oral pathogen associated with multiple cancers, has limited research on its role in oral squamous cell carcinoma (OSCC). This study shows that *P. micra* is enriched in OSCC tissues and positively correlated with tumor metastasis and stages. *P. micra* infection promotes OSCC metastasis by inducing hypoxia/HIF-1α, glycolysis, and autophagy. Mechanistically, *P. micra* surface protein TmpC binds to CKAP4, a receptor overexpressed in OSCC, facilitating bacterial attachment and invasion. This interaction activates HIF-1α and autophagy via CKAP4-RanBP2 and CKAP4-NBR1 pathways, driving metastasis. Targeting CKAP4 with masitinib or antibodies impairs *P. micra* attachment and abolishes *P. micra*-promoted OSCC metastasis in vitro and in vivo. Together, our findings identify *P. micra* as a pathogen that promotes OSCC metastasis and highlight that TmpC-CKAP4 interaction could be a potential therapeutic target for OSCC.

Oral squamous cell carcinoma (OSCC) is a prevalent type of head and neck malignancy, comprising 2% to 4% of all cancer diagnosed[1]. Due to the high rate of metastasis, the 5-year survival rate remains below 50%, despite advancements in the diagnosis and treatment of OSCC[2,3]. Of these, lymph node micrometastasis (LM) is considered the most significant prognostic risk factor for OSCC, serving as the primary reason for the low survival rates observed in OSCC patients[4]. Hence, a comprehensive mechanism study of LM can help to better understand the pathogenesis of OSCC and to identify potential therapeutic targets for OSCC patients.

Recent studies have demonstrated a strong correlation between the microbiota present within tumor tissues and the metastasis of multiple types of human cancers[5–7]. For example, microbes residing in breast tumor-tissue, including *Streptococcus xylosus*, *Lactobacillus animalis*, and *Staphylococcus cuniculi*, promote breast tumor metastasis[8]. *Fusobacterium* (*F.*) *nucleatum* can drive colorectal cancer (CRC) epithelial-mesenchymal transition (EMT) and metastasis by activating TLR4/Keap1/NRF2 signaling pathway[9] or inducing the overexpression of LncRNA EVADR[10]. Likewise, a number of oral pathogenic bacteria are associated with the progression of OSCC[11]. Among them, *Porphyromonas* (*P.*) *gingivalis* promotes OSCC development by modulating tumor-immune microenvironment and activating PI3K-AKT pathway[12,13]; *F. nucleatum* facilitates OSCC EMT and metastasis by activating autophagy and GLUT1-driven lactate production[14,15]. Therefore, revealing how oral pathogen promotes OSCC metastasis is a crucial topic in current studies.

Parvimonas micra (*P. micra*) is not merely an oral opportunistic pathogen that is frequently detected in various oral diseases, including endodontic abscesses, periodontitis lesions, and orofacial odontogenic infections[16,17]. Furthermore, *P. micra* is implicated in the development of various tumor types. For example, *P. micra* promotes CRC development by inducing cell proliferation and altering Th17 immune

[1]Department of Human Microbiome, School and Hospital of Stomatology, Cheeloo College of Medicine, Shandong University & Shandong Key Laboratory of Oral Tissue Regeneration & Shandong Engineering Research Center of Dental Materials and Oral Tissue Regeneration & Shandong Provincial Clinical Research Center for Oral Diseases, Jinan 250012, China. [2]Nanjing Stomatological Hospital, Affiliated Hospital of Medical School, Institute of Stomatology, Nanjing University, Nanjing 210093, China. [3]Department of Endocrinology, Qilu Hospital of Shandong University, Cheeloo College of Medicine, Shandong University, Jinan 250012, China. [4]These authors contributed equally: Houbao Qi, Haiting Gao. e-mail: fengqiang@sdu.edu.cn

response[18,19]. *P. micra* may be involved in the progression of gastric cancer, with significant centrality in the gastric cancer ecological network[20]. However, as one of the commonly opportunistic pathogens in the oral cavity, whether and how *P. micra* plays a role in the progression of OSCC remains unclear.

In this study, we examined the abundance of *P. micra* in OSCC tissues and delved into its function in facilitating OSCC metastasis. We utilized single-cell RNA sequencing (scRNA-seq) to evaluate the impact of *P. micra* on both OSCC and the tumor microenvironment (TME). Subsequently, we pinpointed the *P. micra* surface adhesin and cellular receptor responsible for mediating its tumor-promoting activity, thereby elucidating the underlying intracellular molecular mechanisms. Ultimately, we identified a small chemical compound to confirm the role of the cell receptor in OSCC LM.

Results

P. micra enriched in OSCC tissue and correlated with OSCC metastasis

To examine the relationship between *P. micra* and OSCC, we analyzed the abundance of *P. micra* in OSCC patients using the microbiome data of OSCC tissues, paracancerous tissues and normal oral mucosa (PRJNA866676)[21]. The results showed that *P. micra* was significantly enriched in OSCC tissues compared with paracancerous tissues and normal oral mucosa (Fig. 1a). Its abundance in metastatic OSCC was significantly higher than that in non-metastatic OSCC (Fig. 1b). Compared with paracancerous tissues, the abundance of *P. micra* consistently increased in OSCC patients from stage 1 to stage 3 (Fig. 1c). Next, RNA sequencing data (GSE227919)[22] derived from OSCC versus paracancerous tissues was used to validated the enrichment of *P. micra* in OSCC tissue. The microbial communities of OSCC and paracancerous tissues were significantly different (Fig. 1d) and *P. micra* was enriched in OSCC tissues (Fig. 1e). In addition, the potential cellular functions of *P. micra* was examined by pathway enrichment analysis, which found that multiple oncogenic pathways, such as autophagy of mitochondrion, canonical Wnt and cell growth, were positively correlated with the abundance of *P. micra* (Supplementary Fig. 1a). Gene set variation analysis (GSVA) also showed that several gene sets, including Nod-like receptor signaling and pathogenic infection activation pathways in OSCC, were positively correlated with the abundance of *P. micra*, while tight junction was negatively correlated with *P. micra* (Supplementary Fig. 1b). Moreover, the abundance of *P. micra* was positively correlated with the expression of the genes that involved in tumor progression, such as *TWIST1*[23], *GLUT1*[24] and *LDHA*[25] (Supplementary Fig. 1c).

To visualize the enrichment of *P. micra* in OSCC tissues, fluorescence in situ hybridization (FISH) assay used a FITC-labeled *P. micra*-specific probe was conducted. Consistently, *P. micra* was enriched in the metastasized OSCC tissue compared with that in the OSCC lesion without metastasis (Fig. 1f, g). As tumor metastasis is facilitated by EMT, the abundance of *P. micra* and EMT markers was explored by FISH and immunofluorescence (IF) assay, respectively. The results showed that the abundance of *P. micra* was negatively correlated with the expression of E-cadherin while positively correlated with N-cadherin (Fig. 1h–k). Overall, these results suggest that *P. micra* may involve in the EMT and metastasis of OSCC.

P. micra promoted OSCC metastasis

To determine the impact of *P. micra* on OSCC metastasis in vitro, two different OSCC cell lines, CAL27 and SCC15, were cultured with *P. micra* to examine cell proliferation and metastasis, respectively. The results showed *P. micra* slightly promoted OSCC cell proliferation at low MOI (Supplementary Fig. 2a), while dramatically accelerated cell migration and invasion in a dose-dependent manner (Fig. 2a, b and Supplementary Fig. 2b, c). The expression of EMT markers in CAL27 and SCC15 cells with/without *P. micra* infection (MOI = 100) was analyzed, which showed that E-cadherin was markedly decreased by *P. micra* infection, while N-cadherin was dramatically upregulated (Fig. 2c, d and Supplementary Fig. 2d). These results demonstrate that *P. micra* potentiates OSCC metastasis in vitro.

Next, a mouse oral cancer model was established by the implantation of Luc-CAL27 cells with/without *P. micra* infection on the left lateral edge of the tongue (Fig. 2e). The size tumor and cervical lymph nodes (cLNs) of the *P. micra*-treated group was significantly larger than that of the control group (Fig. 2f, g). CK5/6 staining showed *P. micra* increased the presence of OSCC cells in the cLNs (Fig.2h, i). Furthermore, the expression of E-cadherin in *P. micra*-treated OSCC tissue was lower, while N-cadherin was significantly upregulated (Fig. 2j, k). These results indicate that *P. micra* enhances OSCC EMT and metastasis in vivo.

To elucidate how *P. micra* promote OSCC metastasis, we performed scRNA-seq of the orthotopic CAL27 OSCC tumors with/without *P. micra* infection (Fig. 2l). A total of 49,765 single tumor cells were successfully characterized and classified into 6 separate clusters using non-negative matrix factorization (NNMF), and visualized by uniform manifold approximation and projection (UMAP, Fig. 2m). Clusters 2 and 3 exhibited a specific set of cell cycle-related genes indicative of the G1/S and G2/M phases, respectively (Fig. 2n). Cluster 4 was characterized with epithelial differentiation biomarkers, including KRT16, KRT6B, S100A7/8/9. Cluster 6 exhibited the highest activity in immune-related pathways, including TNF-α signaling, complement, and inflammatory response (Supplementary Fig. 3a). While Cluster 5 highly expressed genes associated with ECM (MMP1/10/13) and receptor of E-cadherin (ITGA2), which exhibited the higher activity in EMT related functions, including epithelial-mesenchymal transition, Wnt/β-catenin signaling, glycolysis and hypoxia (Supplementary Fig. 3a-d). Notably, *P. micra* increased the cell proportion of Cluster 5 compared with the control group (Supplementary Fig. 3e), suggesting *P. micra* may promoted OSCC LM via regulating EMT-related signaling pathways. Additionally, GSVA showed that the carcinogenic pathways, including Glycolysis, PI3K-AKT-mTOR, Hypoxia, and EMT, were significantly activated in all tumor cells from *P. micra*-treated group (Fig. 2o).

Next, we clustered TME cells into six clusters by typical cell markers, which involved monocyte-macrophage, fibroblast, endothelial, neutrophil, dendritic and epithelial cells (Supplementary Fig. 4a, b). Odds ratios (OR) analysis showed that *P. micra*-treated group enriched in monocyte-macrophage, fibroblast, and endothelial cells in comparison to control group (Supplementary Fig. 4c). CellChat analysis was conducted to evaluate the interactions among six major TME components, which showed that *P. micra* markedly modified the overall interaction, especially enhanced the interaction between fibroblasts and other TME cells excluding epithelial cells (Supplementary Fig. 4d). For instance, *P. micra* promoted the crosstalk between fibroblasts and monocyte-macrophage through the Ccl7/8-Ccr1/2 interaction (Supplementary Fig. 4e). These results suggest that fibroblast is an important cell type in *P. micra*-regulated OSCC TME.

Five subtypes of cancer-associated fibroblasts (CAFs) were identified as well as normal fibroblasts (NFs) and smooth muscle cells (SMCs) (Supplementary Fig. 4f–g). *P. micra*-treated group was enriched in cancer-associated myofibroblasts (myCAFs) and antigen-presenting CAFs (apCAFs) in comparison to control group (Supplementary Fig. 4h). *P. micra* increased the expression of carcinogenic pathways, including angiogenesis, EMT and PI3K-AKT-mTOR in myCAFs (Supplementary Fig. 4i), and activated the immune-related pathways in apCAFs, including complement, inflammatory response and IL2-STAT5 signaling pathways (Supplementary Fig. 4j). These results suggest that *P. micra* may reshape CAFs in OSCC tissues.

Tumor-associated macrophages (TAMs) are the most abundant immune cells in the OSCC TME (Supplementary Fig. 4a). The subpopulation of monocyte-macrophage cells was characterized and

https://doi.org/10.1038/s41467-025-57530-1

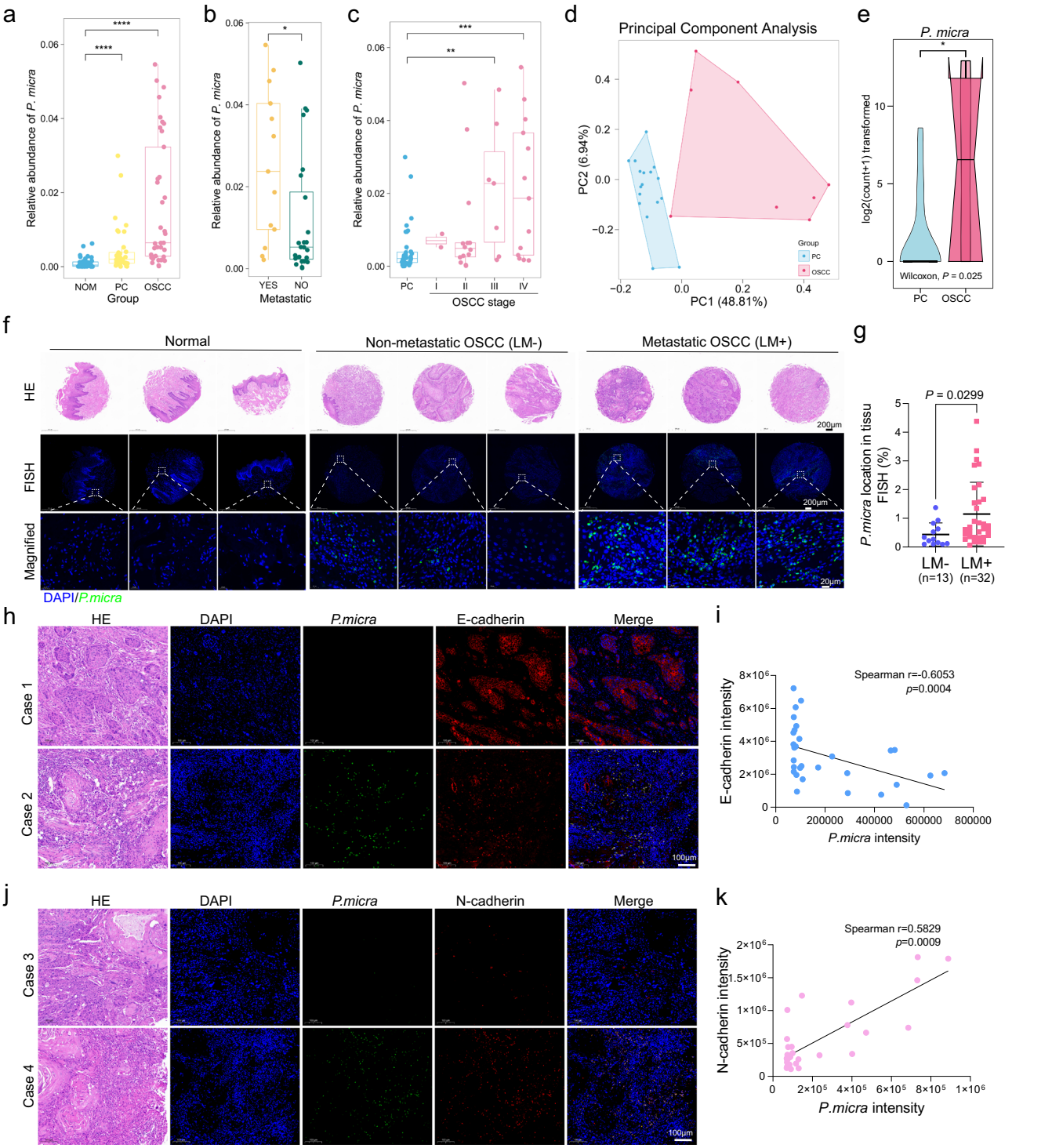

Fig. 1 | *P. micra* enriched in OSCC tissue and correlated with OSCC metastasis. **a** The abundance of *P. micra* in OSCC tissue ($n = 37$ samples), paracancerous tissue (PC, $n = 37$ samples) and anatomically matched contralateral normal oral mucosa (NOM, $n = 38$ independent samples) was plotted in microbiome data. PC vs NOM, $P < 0.0001$; OSCC vs NOM, $P < 0.0001$. **b** Relative abundance of *P. micra* in OSCC tissues with ($n = 13$ samples) or without ($n = 23$ samples) metastasis. $P = 0.018$. **c** Relative abundance of *P. micra* in different stage of OSCC (PC, $n = 37$ samples; I: T1 N0 M0, $n = 2$ samples; II: T2 N0 M0, $n = 13$ samples; III: T1-2 N1 M0 and T3 N0-1 M0, $n = 7$ samples; IV: T1-3 N2 M0 and T4a N0-2 M0, $n = 13$ samples. III vs PC, $P = 0.0056$; IV vs PC, $P = 0.0007$). **d** PCoA showing bacterial community variations between paracancerous tissue (PC) and OSCC tissues (GSE227919 dataset). The lower and upper hinges of the box represent the 25th and 75th percentiles, and the whiskers extend to the minimum and maximum values within 1.5 times the interquartile range. The median value is depicted by the line within the box (**a**-**c**). **e** The abundance of *P. micra* in PC ($n = 17$ samples) and OSCC tissue ($n = 8$ samples) of GSE227919 datase. **f** and **g** Representative images (**f**) and quantification analysis (**g**) of *P. micra* distribution by FISH staining (Green: *P. micra*) in normal tongue samples ($n = 9$ samples), non-metastatic ($n = 13$ samples) or metastatic ($n = 32$ samples) OSCC tissues. **h** and **i** Representative images (**h**) and Spearman correlation analysis (**i**) of *P. micra* and E-cadherin in OSCC tissue ($n = 30$ samples). **j** and **k** Representative images (**j**) and Spearman correlation (**k**) of *P. micra* and N-cadherin in OSCC tissue ($n = 30$ samples). Scale bar: 100 μm. Data were presented as the means ± SD. Two-sided Wilcoxon test (**a**–**c**, **e**), two-sided unpaired Student's t test (**g**) and two-sided spearman test (**i**, **k**) were used to examine the statistical significance between groups.

https://doi.org/10.1038/s41467-025-57530-1

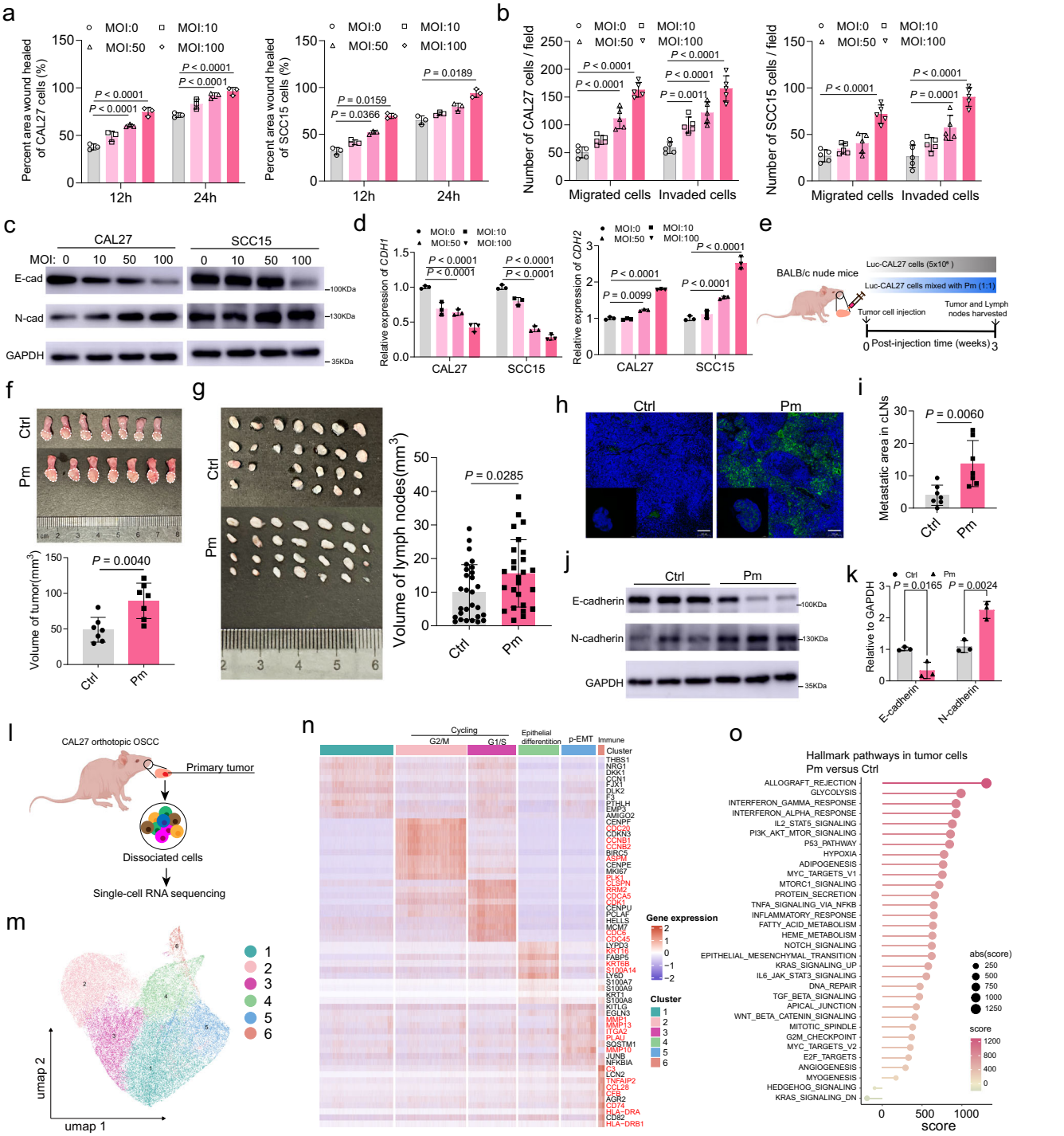

Fig. 2 | *P. micra* promoted OSCC metastasis in vitro and in vivo. a Wound-healing migration assay of OSCC cells co-cultured with *P. micra* in different MOI ($n = 3$ biological replicates per group). **b** Trans-well assays of OSCC cell pre-exposed with *P. micra* for 12 h in different MOI. The indicated migrated and invaded cells were quantified in five randomly selected fields. **c** Western blot assay of E-cadherin (E-cad) and N-cadherin (N-cad) in OSCC cells infected with *P. micra* for 24 h. The data are representative of at least two independent experiments with similar results. **d** qPCR assay of *CDH1* and *CDH2* ($n = 3$ biological replicates in each group) in OSCC cells stimulated with *P. micra* for 24 h. **e** BALB/c nude mice were implanted with Luc-CAL27 or *P. micra* stimulated Luc-CAL27 cells on the left lateral edge of the tongue for 3 weeks. **f** Images of tongue and quantification of tumor volume ($n = 7$ mice per group). **g** Images of cervical lymph nodes (cLNs) and quantification of cLNs volume in vivo from 7 mice per group. **h** and **i** Representative images of immunofluorescence for CK5/6 (**h**) and quantification of metastatic area (**i**) in cLNs in vivo ($n = 7$ mice per group). Scale bar: 100 μm. **j** and **k** Western blot (**j**) and quantification (**k**) of E-cadherin and N-cadherin in CAL27 tumors in vivo ($n = 3$ mice per group). **l** Schematic diagram of single-cell RNA sequencing analysis of tumor cells from orthotopic CAL27 tumor model. **m** NNMF and UMAP of tumor cells. **n** Heatmap showed the differently expressed genes identified by NNMF. The corresponding gene signatures were numbered and selected genes indicated (red). **o** GSVA showing differences in hallmark pathways in tumor cells between *P.micra*-exposed tumors and control group. Data were presented as the means ± SD. One-way ANOVA with Turkey's test (**a**, **b**, **d**, **k**) and two-sided unpaired Student's t test (**f**, **g**, **i**) were used to examine the statistical significance between groups. The samples derive from the same experiment but different gels for E-cadherin, another for GAPDH and N-cadherin were processed in parallel (**c**, **k**).

identified 1 monocyte and 4 TAM subtypes (Supplementary Fig. 4k, l). *P. micra* increased the abundance of monocytes and activated the pathways of immune regulation, such as leukocyte transendothelial migration, chemokine signaling pathway, and cytokine-cytokine receptor interaction in monocytes (Supplementary Fig. 4m, n). These results indicate that *P. micra* may reshape the TAMs to promote OSCC metastasis.

P. micra promoted OSCC metastasis through HIF-1α-induced glycolysis and autophagy

To clarify the pathways involved in *P. micra*-promoted OSCC metastasis, we performed RNA-seq analysis on CAL27 with/without *P. micra* infection (MOI = 100). KEGG enrichment analysis revealed the upregulation of multiple oncogenic pathways, including HIF-1, NOD-like receptor, Glycolysis, and NF-κB in CAL27 cells stimulated with *P. micra* (Supplementary Fig. 5a). GSVA also showed that HIF-1 signaling pathway and Glycolysis/Gluconeogenesis were significantly activated by *P. micra*-infection (Fig. 3a).

P. micra-induced hypoxia was verified using the Image-iT Green Hypoxia Reagent (Fig. 3b, Supplementary Fig. 5b). Consistently, *P. micra* significantly upregulated the expression of HIF-1α in OSCC cells, while having no effect on HIF-2α (Fig. 3c, Supplementary Fig. 5c). Heat inactivated *P. micra* also increased the expression of HIF-1α (Supplementary Fig. 5d), indicating HIF-1α induced by *P. micra* is independent of intracellular *P. micra*. FISH and immunofluorescence (IF) analysis showed that the abundance of *P. micra* was positively correlated with the expression of HIF-1α in OSCC tissues (Supplementary Fig. 5e).

Next, glycolysis was evaluated by comparing the expression of glycolytic proteins, and the levels of glucose uptake and lactate output in OSCC cells with/without *P. micra* infection (MOI = 100). The results showed that *P. micra* simultaneously elevated the expression of GLUT1, HK2 and PFKFB3 (Fig. 3c, d and Supplementary Fig. 6a, b), and significantly promoted glucose uptake and lactate output (Fig. 3e, f). These results indicate that *P. micra* activates glycolysis in OSCC cells.

As a transcription factor, HIF-1α could promote the expression of glycolytic proteins, such as HK2, PFKFB3, and GLUT1 to active glycolysis[26]. We tested whether *P. micra*-induced glycolysis was regulated by HIF-1α. Firstly, we compared the expression of HIF-1α and glycolytic proteins in OSCC cells with dimethyloxalylglycine (DMOG, a HIF stabilizer)[27], *P. micra*, or DMOG + *P. micra*. The expression of HIF-1α induced by *P. micra* at an MOI of 100 was comparable to that elicited by a 0.5 mM concentration of DMOG (Supplementary Fig. 7a). DMOG alone elevated the expression levels of HK2, GLUT1, and PFKFB3, and in combination with *P. micra*, the expression of these proteins displayed an additive upregulation effect (Fig. 3d and Supplementary Fig. 6b). The small interfering RNAs targeting HIF-1α (siHIF-1α) or inhibiting HIF-1α by LW6[28] markedly reduced the expression of glycolytic proteins induced by *P. micra*, including HK2, GLUT1, and PFKFB3 (Fig. 3g and Supplementary Figs. 6c, 7b). This was accompanied by a reduction in glucose uptake and lactate production (Fig. 3e, f and Supplementary Fig. 7c). These results suggest that *P. micra*-promoted glycolysis is regulated by HIF-1α in OSCC cells.

Besides, RNA-seq analysis on CAL27 cells also showed that a group of autophagy genes were upregulated by *P. micra* infection (Supplementary Fig. 8). Transmission Electron Microscope (TEM) showed a significant increase of autophagosomes in *P. micra*-exposed CAL27 and SCC15 cells compared to non-exposed cells (Fig. 3h). Western blot also showed an increased expression of the autophagy marker LC3B II by *P. micra* infection, whereas P62 was decreased (Fig. 3i and Supplementary Fig. 9a). CAL27 and SCC15 cells were transfected with mRFP-GFP-LC3 adenoviruses to evaluate the autophagic flux. Confocal fluorescence microscope showed that *P. micra* significantly enhanced the autophagic flux indicated by the increased number of autophagosome and autolysosome (Fig. 3j). These results suggest that *P. micra* can activate the autophagy of OSCC cells.

Hypoxia/HIF-1α can induce autophagy[29] and glycolysis can also facilitate autophagy in response to glucose deprivation[30,31]. Therefore, whether *P. micra*-activated autophagy could be regulated by HIF-1α and/or glycolysis was investigated. DMOG increased the protein level of LC3BII while decreased the expression of P62 (Fig. 3k and Supplementary Fig. 9b). siHIF-1α and LW6 as well as 2-DG (glycolysis inhibitor) dramatically inhibited the *P. micra*-induced autophagic flux and rescued the expression of LC3B II and P62 in both CAL27 and SCC15 cells (Fig. 3l, m and Supplementary Figs. 9c–d, 10a–c). These results imply that *P. micra*-induced autophagy in OSCC cells is regulated by HIF-1α and glycolysis.

Next, we investigated whether *P. micra* induced OSCC metastasis was mediated by HIF-1α, glycolysis and autophagy. siHIF-1α, LW6 or 2-DG abolished the effect of *P. micra* on OSCC cell migration and invasion, respectively (Supplementary Fig. 11a–d). The expression of N-cadherin and E-cadherin induced by *P. micra* were also rescued by LW6 and 2-DG, respectively (Supplementary Fig. 11e). The autophagy inhibitor, CHQ, abolished the effect of *P. micra* on migration and invasion in both CAL27 and SCC15 cells (Supplementary Fig. 11f, g). Also, CHQ rescued the expression of E-cadherin and N-cadherin induced by *P. micra* (Supplementary Fig. 11h). The above results indicate that *P. micra* promotes the OSCC metastasis by activating HIF-1α, glycolysis and autophagy.

To further verify the role of HIF-1α in *P. micra*-promoted OSCC metastasis in vivo, CAL27 cells, and CAL27 cells transfected by siHIF-1α with/without *P. micra* infection were implanted on the tongue of mice model, respectively. The results showed that siHIF-1α + *P. micra* group displayed smaller size of tumors and cLNs as well as lower tumor cell metastatic area in cLNs compared to the *P. micra* group (Supplementary Fig. 12). These results suggest that HIF-1α is an important mediator of *P. micra*-promoted OSCC metastasis.

TmpC was an effector of *P. micra* promoted OSCC metastasis

As the surface and intra-cellular of CAL27 and SCC15 cells contained amounts of live *P. micra* (Supplementary Fig. 13a), suggest *P. micra* may exert its pathogenicity by adhering and invading OSCC cells. Scanning electron microscopy (SEM) and TEM confirmed the attachment and invasion of *P. micra* to OSCC cells (Fig. 4a, b). CFSE-labeled *P. micra* was also observed on the surface and plasma of CAL27 and SCC15 cells by confocal microscopy (Supplementary Fig. 13b). These results suggest that *P. micra* may exert its pathogenic effects to OSCC cells by the surface proteins.

To elucidate the mechanism responsible for *P. micra* attachment and invasion to OSCC cells, we focused on *P. micra* surface protein TmpC, which was an important adhesins of *P. micra*. TmpC was obtained and used to simulate OSCC cells, which showed that TmpC significantly promoted the migration and invasion of OSCC cells (Fig. 4c, d and Supplementary Fig. 14a, d), and induced cell hypoxia (Fig. 4e, Supplementary Fig. 14c) in both CAL27 and SCC15 cells. The expression of HIF-1α, HK2 and LC3B II was upregulated by TmpC (Supplementary Fig. 14d, e). TmpC significantly increased the mRNA level of glycolytic proteins, such as HK2, LDHA, PFKFB4 (Supplementary Fig. 14f), albeit to a lesser extent compared to *P. micra*. Furthermore, HIF-1α served as a pivotal mediator in TmpC-induced glucose uptake and lactate production in OSCC cells (Supplementary Fig. 14g). These results indicate that TmpC is an important virulence effector of *P. micra* promoted OSCC metastasis.

To validate the essential role of TmpC, we utilized insertional inactivation (Fig. 4f) to generate a TmpC mutant strain (PmΔ*tmpC*, Fig. 4g). Compared with wild-type *P. micra* (PmWT), PmΔ*tmpC* demonstrated a significant reduction in the adhesion and invasion abilities to OSCC cells in vitro (Fig. 4h) and was unable to elicit LM of OSCC in vivo (Fig. 4i–o). Together, these results suggest that TmpC is the necessary effector of *P. micra* to promote OSCC metastasis in vivo.

https://doi.org/10.1038/s41467-025-57530-1

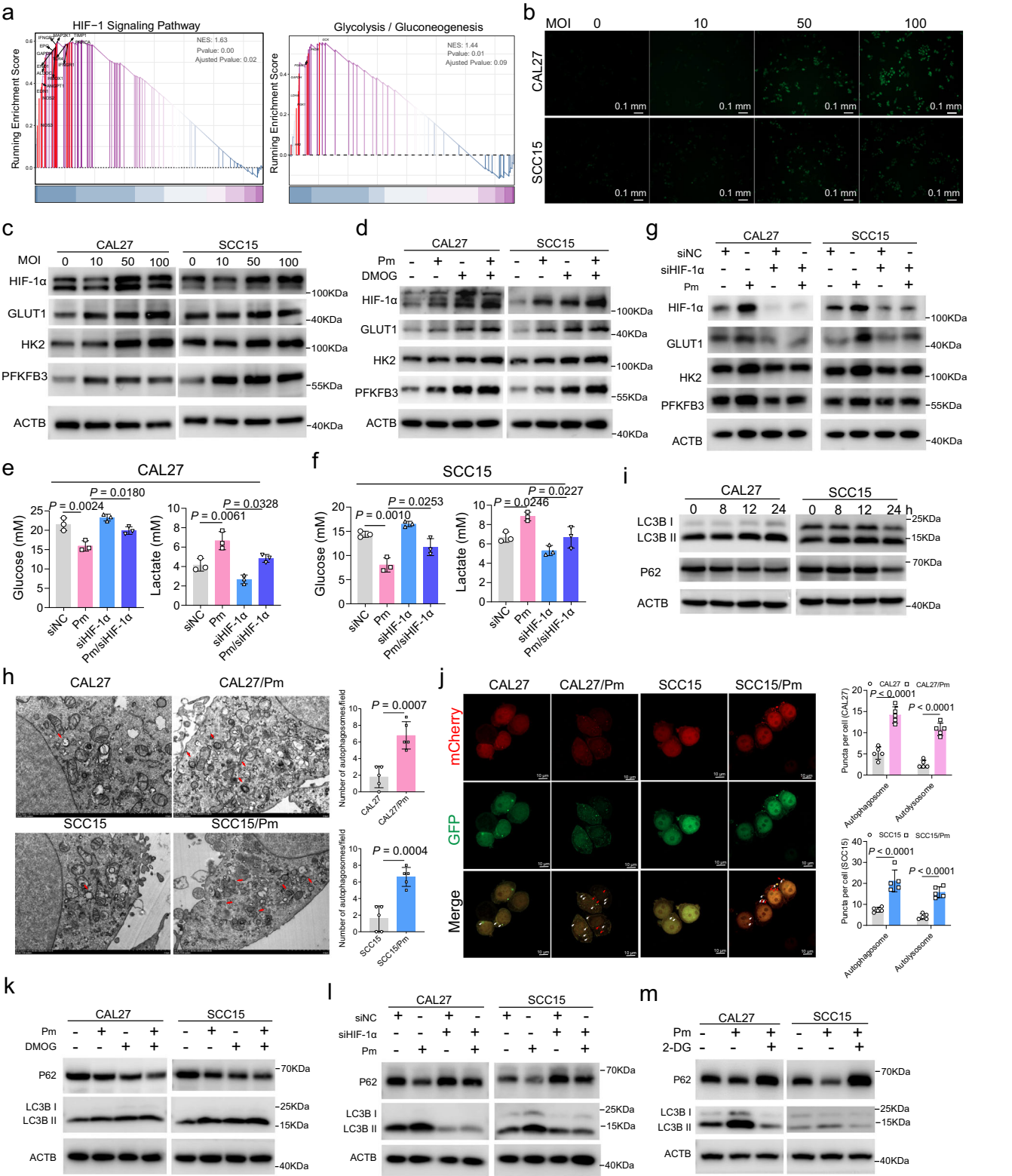

TmpC interacted with CKAP4 to promote OSCC metastasis

The receptor of TmpC on OSCC cells was analyzed by His-tagged TmpC and HLPC-MS from both CAL27 and SCC15 cells (Fig. 5a). CKAP4, a type II transmembrane protein, was identified as one of the TmpC receptors by overlapping all candidate proteins detected in both cell lines (Supplementary Table 1). Immunoprecipitation analysis showed CKAP4 could be pulled down by His-TmpC in both CAL27 and SCC15 cells (Fig. 5b). Confocal fluorescence microscopy showed that CKAP4 was co-localized with CFSE-labeled *P. micra* (Supplementary Fig. 15a). These results indicate that CKAP4 is a receptor of TmpC on OSCC cells.

Next, we investigated the role of CKAP4 in *P. micra*/TmpC promoted OSCC metastasis. Knockdown of CKAP4 by siRNAs (siCKAP4) or blockade of CKAP4 with neutralizing antibodies (CKAP4Ab) markedly inhibited the attachment and invasion of *P. micra* to OSCC cells (Fig. 5c and Supplementary Fig. 15b). siCKAP4 attenuated *P. micra*/TmpC-promoted migration and invasion as well as glucose uptake, lactate output and autophagic flux in OSCC cells (Supplementary

Fig. 3 | *P. micra* activated Hypoxia/HIF-1α, glycolysis and autophagy in OSCC cells. a The GSEA showing the enrichment of HIF-1 signaling pathway and Glycolysis/Gluconeogenesis pathway in *P. micra* stimulated group. The *p*-value is obtained through one-sided permutation test with 1000 permutations. Adjusted *p*-value is the result of multiple validation correction on the original *P*-value. **b** Representative images of the Image-iT Green Hypoxia Reagent analysis. The data are representative of at least two independent experiments with similar results. **c** Western blot of HIF-1α, GLUT1, HK2 and PFKFB3 by *P. micra* infection with different MOI for 24 h. **d** Western blot of HIF-1α, GLUT1, HK2 and PFKFB3 by *P. micra* infection (MOI = 100) and DMOG (1.0 mM) treatment for 24 h. **e** and **f** Glucose and lactate concentration in culture supernatant of CAL27 (**e**) and SCC15 (**f**) transfected with siHIF-1α for 24 h and followed by *P. micra* infection 24 h ($n = 3$ biological replicates in each group). **g** Western blot of HIF-1α, GLUT1, HK2 and PFKFB3 in OSCC cells transfected with siHIF-1α for 24 h and followed by *P. micra* infection 24 h. **h** TEM showing autophagosomes in CAL27 and SCC15 following *P. micra* infection for 24 h ($n = 5$ biological replicates per group). Arrows indicated autophagosome. **i** Western blot of LC3B and P62 after *P. micra* infection 24 h. **j** Representative images and quantification of autophagosome and autolysosome in OSCC cells infected with mRFP-GFP-LC3 adenovirus 24 h and stimulated with *P. micra* for another 24 h ($n = 3$ biological replicates per group). White arrows indicated autophagosomes and red arrows indicated autolysosomes. scale bars, 100μm. **k** Western blot of LC3B and P62 in the presence of DMOG and *P. micra* for 24 h. **l** Western blot showing the impact of siHIF-1α on LC3B and P62. **m** Western blot showing the impact of 2-DG on LC3B and P62. Data were shown as mean ± SD. Blots are representative of at least two biological replicate experiments with similar results (**c**, **d**, **g**, **i**, **k**–**m**). The samples derive from the same experiment but different gels for GLUT1, another for HIF-1α and ACTB, another for HK2 and PFKFB3 were processed in parallel (**c**, **d**, **g**). One-way ANOVA with Turkey's test (**e**, **f**, **j**) and two-sided unpaired Student's t test (**h**) were used to examine the statistical significance between groups.

Figs. 16 and 17). Preincubation of OSCC cells with CKAP4Ab eliminated the stimulatory effects of PmWT on the migration and invasion of OSCC cells, whereas no effect was determined on Pm*ΔtmpC* (Fig. 5d–e). In vivo experiment showed siCKAP4+*P. micra* group displayed smaller size of tumors and cLNs as well as lower tumor cell metastatic area in cLNs compared to the *P. micra* group (Supplementary Fig. 12). Moreover, CKAP4Ab and siCKAP4 inhibited PmWT or TmpC-promoted expression of EMT markers (E-cadherin and N-cadherin), HIF-1α, glycolytic proteins (GLUT1, HK2 and PFKFB3) and autophagy proteins (P62 and LC3 II) in OSCC cells, whereas it had no effect on the Pm*ΔtmpC* (Fig. 5f and Supplementary Fig. 18a–c). Pm*ΔtmpC* could not affect OSCC cells migration and invasion as well as the expression of EMT markers, HIF-1α, glycolytic proteins and autophagy proteins (Fig. 5d–f and Supplementary Fig. 18a). These results suggest that CKAP4 is essential for *P. micra*/TmpC promoted OSCC metastasis.

To reveal the domain of CKAP4 bound to TmpC, GST-tagged full length and truncated forms of CKAP4 were constructed according to the predicted domain architecture bound with TmpC (Fig. 5g, h and Supplementary Fig. 19) and subjected to Surface Plasmon Resonance (SPR) assays. The results revealed that aa 331-475 of CKAP4 containing two sites binds with TmpC (Fig. 5i, j). Furthermore, the OSCC cells with stable silencing of CKAP4 (shCKAP4) were constructed (Supplementary Fig. 18d) and then was transfected with full-length *CKAP4* (*CKAP4*^{WT}) or *CKAP4* mutant lacking the TmpC-binding site (*CKAP4*$^{\Delta 991\text{-}1350}$) for rescue experiments. The expression of E-cadherin, N-cadherin, HIF-1α, HK2, PFKFB3, and LC3B II were effectively rescued by *CKAP4*^{WT} in shCKAP4 OSCC cells, but not by *CKAP4*$^{\Delta 991\text{-}1350}$ (Fig. 5k and Supplementary Fig. 20). *CKAP4*^{WT} also enhanced the migration and invasion capability of shCKAP4 cells stimulated by *P. micra* or TmpC, while not *CKAP4*$^{\Delta 991\text{-}1350}$ (Fig. 5l, m).

TmpC-CKAP4 stabilized HIF-1α by RanBP2 and induced autophagy by NBR1

The gene expression of HIF-1α was unchanged in OSCC cells with *P. micra*/TmpC stimulation (Supplementary Fig. 21a), while the protein level of HIF-1α was markedly increased (Fig. 3), suggesting that *P. micra*/TmpC may promote the translation or stability of HIF-1α. We further deciphered the proteins involved in TmpC-CKAP4-mediated HIF-1α translation or stability. RanBP2, a SUMO (small ubiquitin-like modifier) E3 ligase[32], was identified from the overlap of the candidate proteins interacted with CKAP4 by HPLC-MS in CAL27 cells with *P. micra*/TmpC stimulation (Fig. 6a, Supplementary Table 2). Co-immunoprecipitation (Co-IP) revealed a direct interaction between RanBP2 and CKAP4 (Fig. 6b). RanBP2 may facilitate the SUMOylation process of HIF-1α, thereby enhancing the stability of the HIF-1α protein[33]. Co-IP assay showed HIF-1α could bind with SUMO1 in both CAL27 and SCC15 cells under the stimulation of *P. micra*/TmpC (Fig. 6c). To assess whether SUMOylation primarily accounts for HIF-1α protein stability, the SUMOylation enzymatic cascade was inhibited using TAK981, a specific inhibitor[34]. The results showed that TAK981 significantly decreased the abundance of HIF-1α and HK2 in CAL27/SCC15 cells under the stimulation of *P. micra*/TmpC (Fig. 6d and Supplementary Fig. 21b). Moreover, siRanBP2 suppressed TmpC-induced stability of HIF-1α (Fig. 6e and Supplementary Fig. 21c). siRanBP2 or TAK981 attenuated *P. micra*-induced up-regulation of LC3BII and down-regulation of P62 (Supplementary Fig. 21d). These results suggest that RanBP2-dependent SUMOylation is involved in the stability of HIF-1α.

Meanwhile, HPLC-MS data also showed the autophagy proteins NBR1 and SQSTM1(P62) were interacted with CKAP4 in CAL27 cells under the stimulation of *P. micra*/TmpC (Fig. 6a). The interaction of NBR1 and CKAP4 was confirmed by Co-IP in CAL27 and SCC15 cells with *P. micra*/TmpC stimulation, respectively (Fig. 6f). Different from NBR1, P62 could bind with CKAP4 in CAL27 or SCC15 cells with/without *P. micra*/TmpC stimulation (Fig. 6g). The knockdown of NBR1 by siRNA (siNBR1) inhibited TmpC-induced autophagy, as evidenced by the restoration of P62 and LC3B II expressing levels (Fig. 6h and Supplementary Fig. 21e). These results indicate that NBR1 is a main mediator involved in TmpC-CKAP4 induced autophagy.

The mechanism by which NBR1 regulates TmpC-CKAP4 induced autophagy was further examined. As a P62-interacting protein, NBR1 enhanced the formation of P62 bodies[35]. Confocal fluorescence microscopy revealed that TmpC stimulation led to a dramatically increase in the quantity of P62 bodies in both SCC15 and CAL27 cells, whereas siNBR1 resulted in a decrease in the number of P62 bodies (Fig. 6i and Supplementary Fig. 21f). Moreover, siCKAP4 increased the protein levels of P62 and NBR1 in both SCC15 and CAL27 cells under the stimulation of TmpC (Supplementary Figs. 18b and 21g), indicating that CKAP4 contributed to the TmpC-induced degradation of P62 and NBR1. Similarly, siCKAP4 inhibited TmpC-induced P62 bodies and the co-localization of P62 and NBR1 (Fig. 6j–l). These results suggest that, with the stimulation of TmpC, CKAP4 promotes NBR1 binding to P62, facilitating the formation of P62 bodies, thereby induce OSCC cell autophagy (Fig. 6m).

Blockade of CKAP4 attenuated *P. micra*/TmpC-promoted OSCC metastasis

To further validate the role of CKAP4 in *P. micra*/TmpC-promoted OSCC metastasis, the small chemicals targeting CKAP4 were selected through molecular docking-based virtual screening and identified 9454 compounds with promising scores (Supplementary Table 3). Considering various factors, four compounds including imidurea, masitinib, fostamatinib, and quizartinib, were chosen for the following experiments (Fig. 7a). Concentrations of these chemicals that had no effect on OSCC cell viability were selected (Supplementary Fig. 22a), subsequently enabling the performance of bacterial attachment/invasion assays. Three chemicals (imidurea,

https://doi.org/10.1038/s41467-025-57530-1

masitinib, and fostamatinib), particularly masitinib, effectively suppressed the attachment and invasion of *P. micra*. However, their efficacy was negated in the presence of siCKAP4 (Fig. 7b-c). Masitinib effectively inhibited the motility of OSCC cells promoted by *P. micra* through a scratching test (Fig. 7d and Supplementary Fig. 22b) and influenced the expression of EMT markers (Supplementary Fig. 22c).

Next, we established an OSCC orthotopic xenograft therapy model to investigate the therapeutic effect of masitinib targeting CKAP4 in vivo, with CKAP4Ab as a positive control (Fig. 7e). Consequently, *P. micra* increased tumor and lymph node size, bioluminescence in tumors and cLNs, and promoted OSCC LM, while CKAP4Ab or masitinib treatment dramatically inhibited the *P. micra*-promoted OSCC metastasis (Fig. 7f–l). The combination therapy of masitinib with

Fig. 4 | *P. micra* interacted with OSCC cells via its surface protein TmpC. **a** Representative SEM images of CAL27 and SCC15 cells after co-culture with *P. micra* (MOI = 100). The higher magnification images showed attachment between bacteria and the cells. **b** Representative TEM images of CAL27 and SCC15 cells after co-culture with *P. micra* (MOI = 100. Red arrows indicated intracellular *P. micra* and white arrows indicated cell-surface *P. micra*. **c** Wound-healing migration assays of OSCC cell stimulated with TmpC (0.05 and 0.1 mg/mL) for 24 h ($n = 3$ biological replicates per group). Scale bar: 100 μm. **d** Trans-well assays of OSCC cells pre-stimulated with TmpC (0.05 and 0.1 mg/mL) for 24 h ($n = 5$ biological replicates per group). Scale bar: 100 μm. **e** Representative images of the Image-iT Green Hypoxia Reagent assay of OSCC cell stimulated with TmpC for 24 h. **f** The schematic representation of the insertional inactivation of TmpC in *P. micra*. DNA fragment containing *ermB* gene was constructed and transformed into *P. micra* wild type (PmWT) for homologous recombination. **g** PCR of insertion mutants of PmWT. Bacteria chromosomal DNA was used as template for the PCR and different primers indicated in (**f**) were used to validate *ermB* insertion. **h** PmΔ*tmpC* showed decreased adhesion and invasion ability compared with PmWT ($n = 3$ biological replicates per group). **i** BALB/c nude mice were implanted with PmWT or PmΔ*tmpC* treated CAL27 cells on the left lateral edge of the tongue for 3 weeks. **j** and **k** Images of tongue (**j**) and quantification of tumor volume (k, $n = 8$ mice per group). **l** and **m** Representative images of cLNs (**l**) and quantification of volume quantification of cLNs volume (**m**) from 8 mice per group. **n** and **o** Representative images of immunofluorescence for CK5/6 (**n**) and quantification of metastatic area (**o**, $n = 8$ mice per group) in cLNs. Scale bar: 500 μm for 2X and 100 μm for 10X. Images are representative of two independent experiments (**a**, **b**, **e**, **g**). Data were shown as mean ± SD. One-way ANOVA with Turkey's test (**c**, **d**, **k**, **m**, **o**) and two-sided unpaired Student's t test (**h**) were used to examine the statistical significance between groups.

CKAP4Ab (Pm/CKAP4Ab/ masitinib group) failed to yield superior therapeutic outcomes in comparison to either CKAP4Ab or masitinib monotherapy (Fig. 7f–l). Additionally, CKAP4Ab or masitinib abolished *P. micra*-induced expression of EMT markers (E-cadherin and N-cadherin), HIF-1α, glycolytic proteins (GLUT1, HK2 and PFKFB3) and autophagy protein (P62) in mice OSCC tissues (Fig. 7m and Supplementary Fig. 23). These results offer additional proof that CKAP4-serves as the primary mediator through which *P. micra*/TmpC exerts its pathogenic influence on OSCC.

We further explored the relationship between *P. micra* and CKAP4 in OSCC patients by FISH and IF assay. Spearman correlation showed that the abundances of *P. micra* was positively correlated with the expression of CKAP4 in OSCC tissues (Fig. 7n, o). RNA-seq data from the TCGA-HNSCC cohort and GEO database (GSE42743)[36] concordantly showed that CKAP4 was markedly higher in OSCC tissues compared to adjacent normal tissues (Fig. 7p). The survival rate analysis of OSCC patients from the GSE42743 and GSE41613 dataset[37] showed that the overall survival (OS) rate was significantly lower for CKAP4-overexpressing OSCC patients (Fig. 7q). Moreover, CKAP4 was positively associated with the expression of HIF-1α and N-cadherin while negatively associated with E-cadherin in OSCC patients (Supplementary Fig. 24). These results suggest that CKAP4 serves as a promising target for OSCC therapy.

Discussion

OSCC exhibited a significant association with the presence of various oral bacteria, such as *P. gingivalis*, *F. nucleatum*, and *Streptococcus specie*[38]. However, previous study rarely focused on the role of *P. micra* in oral cancer. This study demonstrated that *P. micra* is an important pathogen of OSCC.

A study showed *P. micra* can translocate from the subgingival cavity to the gut and promote colorectal tumorigenesis[39]. This process was facilitated by the induction of colonocyte proliferation through the activation of the Ras/ERK/c-Fos signaling pathway[18]. In our study, the abundance of *P. micra* was higher in OSCC tissues from patients with LM than in those from patients without LM. In vivo and in vitro study showed *P. micra* slightly promoted OSCC proliferation while remarkably enhanced OSCC metastatic potential and facilitated LM. Therefore, we focused on how *P. micra* facilitated OSCC metastasis.

The intra tumor tissue provided feasible conditions for the invasion of oral pathogenic bacteria, which in turn promoted tumor progress through various ways[40]. For example, a study on CRC showed *P. micra* induce Th17 immune cells infiltration and expression of Th17 cells-secreted cytokines in the colon, thereby promoting the establishment of a pro-inflammatory microenvironment to favor colorectal tumorigenesis[19]. The scRNA-seq analysis in this study also revealed that *P. micra* alters the OSCC TME to facilitate metastasis by elevating the proportions of CAFs, particularly myCAFs and apCAFs, as well as monocytes, while also activating immune regulatory pathways in these cells and OSCC cells.

Oral pathogenic bacteria can colonize multiple cancer types through specific adhesins. We elucidated TmpC was an essential adhesin and virulence effector of *P. micra* on OSCC cells to facilitate OSCC metastasis. Consistently, studies showed that TmpC is essential for *S. pneumoniae*-related lung infection[41] and for gastric tumorigenesis-promoting effect of *S. anginosus*[42]. However, the extent of HIF-1α-dependent gene induction by TmpC alone was weaker compared to that observed with wild-type *P. micra*. This observation hinted that while TmpC was indeed a prerequisite for this process, additional factors or mechanisms associated with *P. micra* may be required to fully activate HIF-1α signaling. These factors could include other bacterial components, secreted metabolites, or synergistic interactions with host pathways. Next, we proved that TmpC binds to CKAP4 in OSCC cells to mediate the attachment and invasion of *P. micra* to OSCC and promote OSCC metastasis. Importantly, our observation of a positive correlation between CKAP4 expression levels and *P. micra* abundance suggested a potential host-microbe interaction that may contribute to the selective enrichment of *P. micra* in OSCC. CKAP4 was initially identified as a protein resident within the endoplasmic reticulum (ER)[43] which also expressed on the cell membrane of various cells and was an important membrane receptor[44]. Notably, CKAP4 functioned as a receptor for Dickkopf1 (DKK1), and the DKK1/CKAP4 signaling cascade facilitated the proliferation of both normal and cancer cells via the PI3K/AKT signaling pathway[44]. A recent study has revealed that CKAP4 acted as a crucial membrane receptor for the SARS-CoV-2 spike protein[45]. Notably, we demonstrated that the binding site of TmpC to CKAP4 exhibited a high similarity to the active domains of SARS-CoV-2 spike protein (Supplementary Fig. 25). This suggests that CKAP4 possesses considerable potential in mediating pathogen infection within human body.

Mechanically, the combination of CKAP4 and TmpC activates the intracellular signaling cascades in OSCC cells. Specifically, we found that TmpC-CKAP4 could promote SUMOylation of HIF-1α and stabilize HIF-1α protein[33] by SUMO E3 ligase RanBP2[32]. The accumulated HIF-1α in turn activated cellular glycolysis, which facilitated OSCC EMT and metastasis. However, the mechanism by which TmpC alone induced hypoxia was currently unknown and warrants further study. Furthermore, CKAP4 interacted with the autophagy protein NBR1[46], which promoted the formation of P62 bodies and *P. micra*-induced autophagy. Meanwhile, the autophagy activated by *P. micra*/TmpC was enhanced by HIF-1α and glycolysis (Fig. 6m).

The small molecule chemical of Masitinib, targeting CKAP4, was employed to verify whether the pathogenic effects of *P. micra* on OSCC were mainly mediated by CKAP4. Similar to the CKAP4Ab, masitinib abrogated the attachment, invasion, and tumor-promoting effects of *P. micra* on OSCC cells in vitro and inhibited OSCC LM in vivo. In line with our results, masitinib has been investigated in the treatment of pancreatic cancer[47]. Besides, anti-CKAP4 antibody also has shown antitumor activity in pancreatic cancer[48], esophageal

https://doi.org/10.1038/s41467-025-57530-1

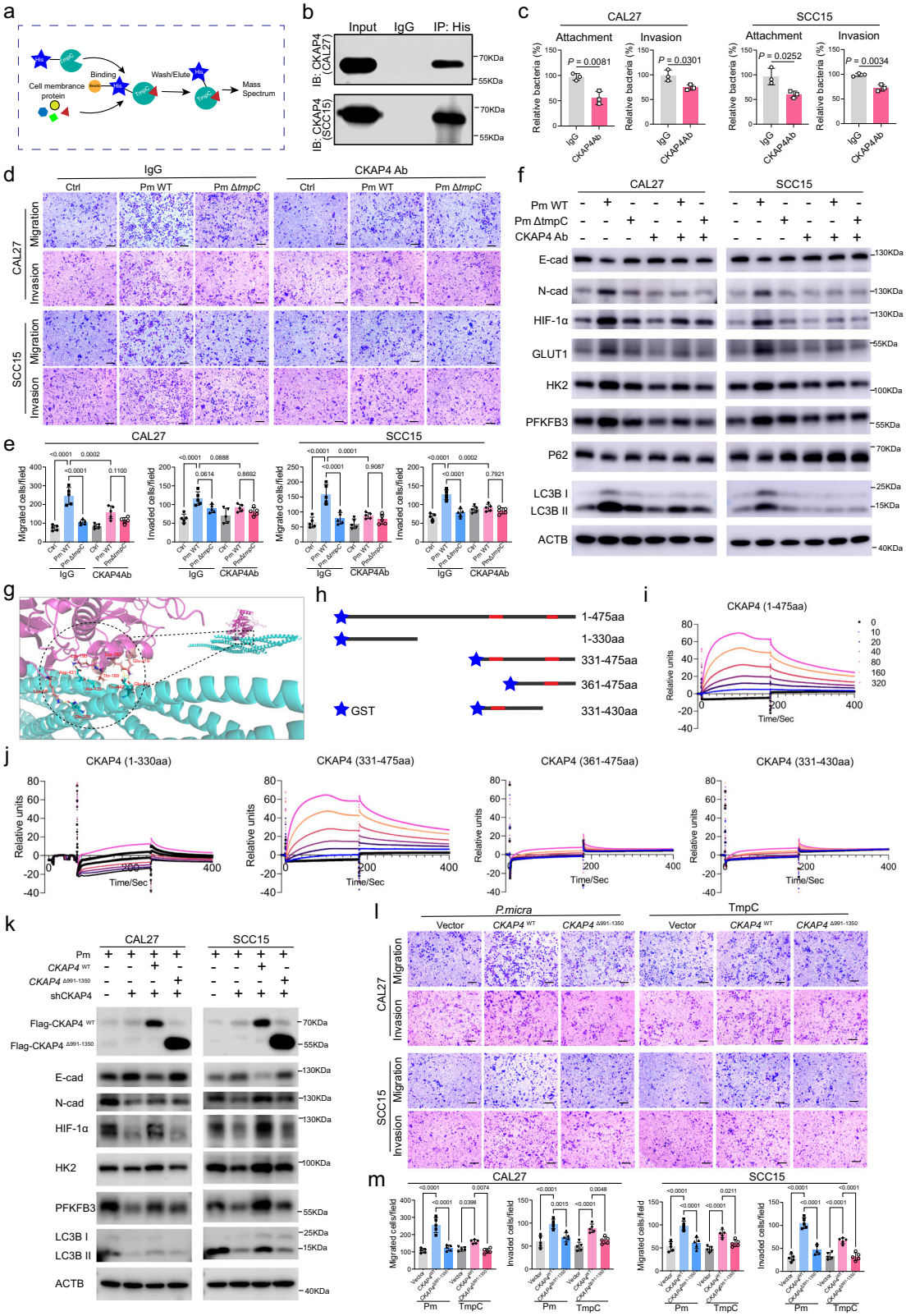

cancer[49], and lung cancers[50]. Collectively, these results exhibited the potential application of masitinib as a therapeutic strategy for OSCC LM, especially with the present of *P. micra*.

Clinically, CKAP4 was higher in OSCC patients and associated with poor overall survival as well as positively correlated with HIF-1α and EMT in OSCC patients. Our scRNA-seq data analysis revealed that CKAP4 was expressed across all subpopulations of OSCC cells, with particularly high expression levels observed in clusters 1, 2, and 3. Of the OSCC TME, CKAP4 exhibited high level of expression in NFs, mCAFs, and monocytes-macrophages in contrast to other subpopulations. Also, CKAP4 has been characterized as pro-tumor molecule that plays a regulatory role in the progression of multiple cancer types, such as lung cancer[51], esophageal squamous cell carcinoma[52] and hepatocellular carcinoma[53], and regulated the signaling pathways

Fig. 5 | *P. micra* surface TmpC bound to CKAP4 on OSCC cells. a OSCC cell membrane protein was incubated with His-TmpC together with His magnetic beads for His-pull-down assay and mass spectrometry analysis. **b** Immunoprecipitation showing His-TmpC directly bound to CKAP4 in OSCC cells. **c** CKAP4Ab suppressed the attachment and invasion of *P. micra* in OSCC cells ($n = 3$ biological replicates in each group). **d** and **e** Representative images (**d**) and quantitation (**e**) of cell migration and invasion of OSCC cells preincubated with CKAP4Ab and treated by PmWT and Pm*Δtmp*C. The indicated migrated and invaded cells were quantified in five randomly selected fields. Scale bars: 100 μm. **f** Western blot of E-cadherin (E-cad), N-cadherin (N-cad), HIF-1α, GLUT1, HK2, PFKFB3, P62 and LC3B in OSCC cells preincubated with CKAP4Ab and treated by PmWT and Pm*Δtmp*C. The samples derive from the same experiment but different gels for N-cadherin and GLUT1, another for HIF-1α and ACTB, another for HK2 and PFKFB3, another for E-cadherin, P62 and LC3B were processed in parallel. **g** Plausible binding mode of CKAP4 (green) with TmpC (pink) from molecular docking study. **h** Schematic illustration of the full-length CKAP4 protein and the truncated forms of CKAP4 tagged with GST. Red segments indicated predicted binding sites. **i** and **j** SPR binding sensorgrams and affinity fit curves for the interaction of TmpC with CKAP4 in vitro. **k** Western blot of proteins expression in shCKAP4 OSCC cells transfected with full-length *CKAP4* ($CKAP4^{WT}$) or CKAP4 mutant lacking the TmpC-binding site ($CKAP4^{\Delta 991\text{-}1350}$) and stimulated by *P. micra*. The samples derive from the same experiment but different gels for N-cadherin and GLUT1, another for HIF-1α and ACTB, another for HK2 and PFKFB3, another for E-cadherin, P62 and LC3B, another for Flag were processed in parallel. **l** and **m** Representative images (**l**) and quantitation (**m**) of cell migration and invasion of OSCC cells transfected with $CKAP4^{WT}$ and $CKAP4^{\Delta 991\text{-}1350}$ and stimulated by *P. micra* ($n = 5$ biological replicates in each group). Scale bars: 100 μm. Data were shown as mean ± SD. Blots are representative of at least two biological replicate experiments with similar results (**f**, **k**). One-way ANOVA with Turkey's test (**e**, **m**) and two-sided unpaired Student's t test (**c**) was used to examine the statistical significance between groups.

including PI3K/AKT and MAPK1/3. This suggests that CKAP4 may play an important role in the progression and prognosis of OSCC.

Collectively, this study showed *P. micra* was an important intratumor bacterium promoting OSCC LM. *P. micra* surface protein, TmpC, binds to CKAP4 on OSCC cells, thereby triggering *P. micra* attachment, invasion, and the subsequent activated HIF-1α and autophagy signaling by CKAP4-RanBP2 and CKAP4-NBR1 interaction, respectively (Fig. 6m). The blockade of CKAP4 with masitinib or CKAP4ab has potential therapeutic effects on OSCC LM.

Our study has the following limitations. While we have clarified the interaction between *P. micra* and OSCC cells, future research utilizing appropriate models should delve into the effect of *P. micra* on inflammatory factors and the intercellular communication they facilitate among OSCC cells and immune cells. Furthermore, additional studies are essential to conclusively determine whether the impacts of *P. micra* on CAFs and TAMs are CKAP4-dependent. Moreover, the mechanisms underlying the enrichment of *P. micra* in OSCC remain elusive and necessitate further exploration.

Methods

Ethics

This research complies with all relevant ethical regulations approved by the Ethics Committee of the School and Hospital of Stomatology, Cheeloo College of Medicine, Shandong University.

Cell lines

Human OSCC cell lines CAL27 and SCC15 were maintained in DMEM and DMEM/F-12 (Shanghai BasalMedia Technologies), respectively, supplemented with 1% penicillin-streptomycin (Gibco, Washington, USA) and 10% fetal bovine serum (FBS), henceforth referred to as DMEM complete media. Pro. Zhiquan Huang (Sun Yat-Sen University) gifted CAL-27 luciferase-labeled cells (Luc-CAL27) cultured at the same conditions as CAL27 cells.

Bacteria

P. micra ATCC33270 was purchased from the Chinese Academy of Sciences. *P. micra* was maintained in SchaEdler anaerobic broth (BD Biosciences, New Jersey, USA) in an anaerobic tube (80% N2, 10% CO_2 and 10% H_2) and incubated for 3-4 days at 37 °C.

Mouse models

BALB/c nude mice (male, 5-6 weeks) were purchased from the Vital River Laboratory Animal Technology (Beijing, China) and bred at Shandong University Model Animal Center. The stable supply and immunodeficiency characteristics of male homozygous nude mice make them the preferred choice for experiments. The mice were randomly assigned to different groups for the experiments, and no animals were excluded from the analyzes. After a week of adjustable feeding, 5×10^6 CAL-27 luciferase-labeled cells with/without siRNA mixed with *P. micra* (MOI = 1) or PBS in 50 μL of Matrigel and DMEM were implanted into the left tongue edge of BALB/c nude mice. After 3 weeks, cervical LNs and tongue tumors were gathered for imaging, immunofluorescence, histopathology and size measurement to measure the proliferation of tumor cells, LM, and EMT. Tumor and LNs volume (mm^3) = Width $(mm)^2 \times$ length (mm)/2[54]. For drug treatments in vivo, the tongue mucosa of each mouse was injected with 5×10^6 Luc-CAL27 cells. After one week, the mice were randomly assigned to seven groups. Then, they received the following treatments: (1) IgG (50 μg, i.p., twice per week); (2) CKAP4Ab (Santa, 50 μg, i.p., twice per week); (3) Masitinib (30 mg/kg, i.p., daily); (4) *P. micra* (5×10^5, i.t., weekly); (5) *P. micra* + CKAP4Ab; (6) *P. micra*+Masitinib and (7) *P. micra* + CKAP4Ab+Masitinib. After 2 weeks, cervical LNs and tongue tumors were gathered for imaging, immunofluorescence, histopathology and size measurement to measure the proliferation of tumor cells, LM, and EMT.

According to the guidelines (GB/T 35892-2018), the ethics committee specified that the maximal tumor burden is no more than 10% of the body weight of animals and the average diameter is less than 20 mm. During the experiment, the tumor sizes of the mice complied with the regulations. All animal protocols were reviewed and approved by the Ethics Committee of the School and Hospital of Stomatology, Cheeloo College of Medicine, Shandong University (approval no. 20230105). This study adhered to the guidelines outlined in the National Institutes of Health Guide for the Care and Use of Laboratory Animals.

Tissue microarray and fluorescence in situ hybridization (FISH)

Human OSCC tissue microarray (HN054Oc01) was purchased from Zhongke Guanghua Intelligent Biotechnology Co., Ltd. (Xi'an, China, https://www.bioaitech.com/). Use of clinical samples was approved by the Ethical Committee and Institutional Review Board of the School and Hospital of Stomatology, Cheeloo College of Medicine, Shandong University in compliance with ethical standards and patient confidentiality (approval no. 20241339). Informed consent was obtained from all the patients regarding the use of tissue samples. The participants ranged in age from 25 to 81 years, of whom 91 % were male. The basic characteristics of this microarray were provided in Supplementary Table 4. Due to the limited samples available, sex and gender were not considered in the study design.

A FITC-conjugated *P. micra* probe, possessing the sequence 5'-CTGAGCGTCAGTAAAAGTCC-3', was used for detecting the colonization of *P. micra* in tissue microarray. After rehydration and deparaffinization, specimens were treated with Proteinase K and 0.2 N HCl for 10 minutes each. After incubation in a blocking buffer for 2 h at 55 °C, the probe (diluted 1:50 in 35% preheated hybridization buffer for 3 minutes at 88 °C) was added and hybridized overnight at 42 °C in a humid, dark chamber. The specimens were then washed in a Tris-HCl buffer (20 mM, pH 7.2) containing 40 mM

https://doi.org/10.1038/s41467-025-57530-1

a

Con	*P.micra*	TmpC	IgG
CKAP4	CKAP4	CKAP4	-
-	RanBP2	RanBP2	-
-	NBR1	NBR1	-
SQSTM1	SQSTM1	SQSTM1	-

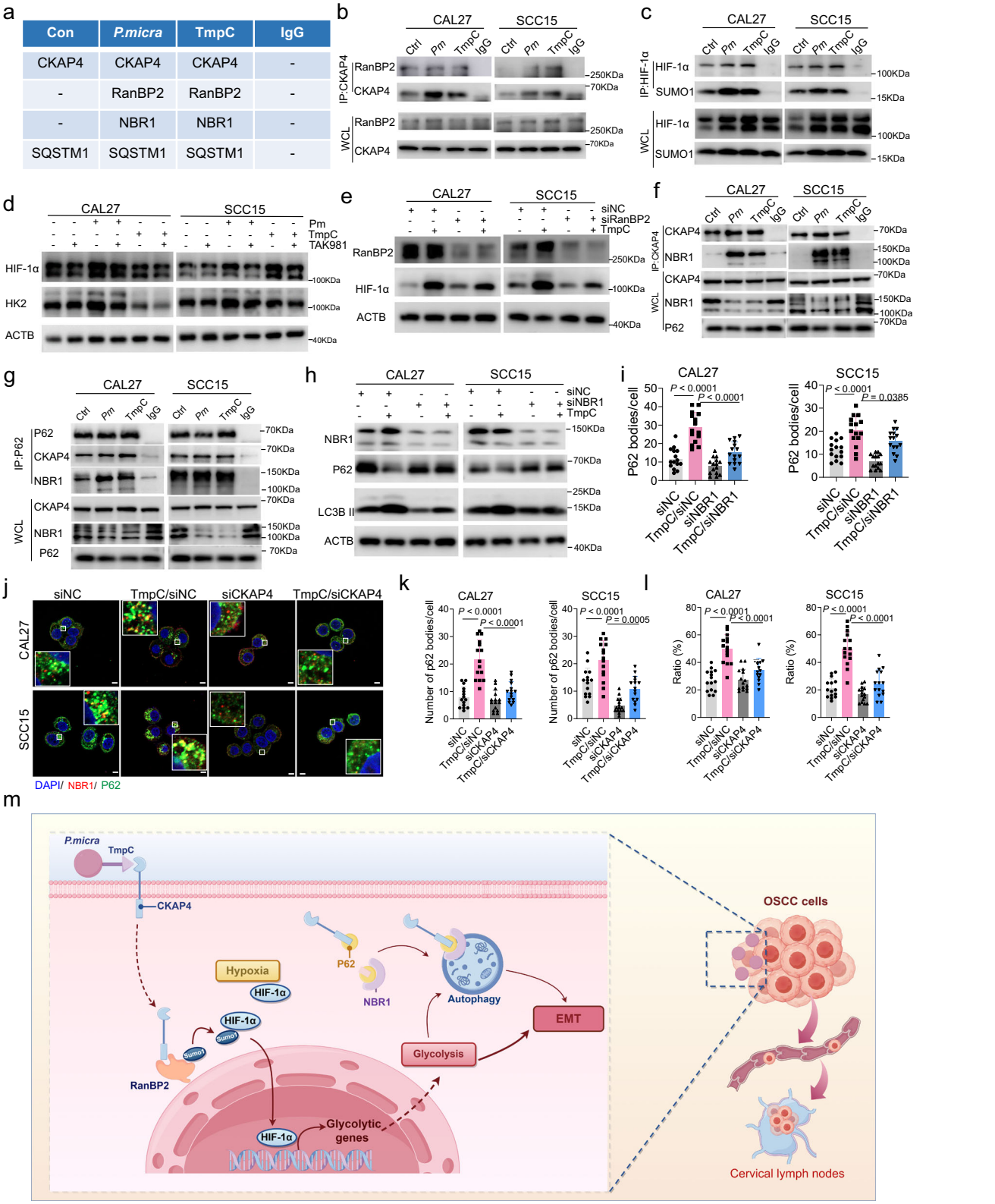

m

NaCl and mounted using a DAPI-antifade solution. The resulting images were captured using Pannoramic 250FLASH. The positive fluorescent signal intensity and area proportion was calculated utilizing ImageJ v1.54 software.

Migration and invasion assay

Trans-well chambers (Corning, 3422) were applied to assess cell migration and invasion. OSCC cells treated with *P. micra* (Indicated MOI or MOI = 100) or stimulated with TmpC (Indicated concentration or 0.1 mg/mL) for 24 h in 6-well plate. In some experiments, the cells were transfected with siRNA 24 h prior to infection. For migration assay, 5×10^4 cells were transplanted along with *P. micra* simultaneously from a 6-well plate into the upper chamber in 200 μl of serum-free medium, while the lower chamber was full of 600 μL medium supplemented with 15% FBS. For invasion assay, the upper chamber was pre-coated with 25 μL of Matrigel (BD, 3422356234). After 24-h

Fig. 6 | TmpC-CKAP4 stabilized HIF-1α by binding RanBP2 and induced autophagy by binding NBR1. a Immunoprecipitation of CKAP4 followed by HPLC-MS identified CKAP4-bound proteins. **b** Co-IP and immunoblotting detection showed the interaction between RanBP2 and CKAP4. **c** Co-IP and immunoblotting detection showed the interaction between HIF-1α and SUMO1. **d** TAK981 decreased the expression of HIF-1α and HK2. The samples derive from the same experiment but different gels for HIF-1α and ACTB, another for HK2 were processed in parallel. **e** siRanBP2 decreased the expression of HIF-1α. **f** Co-IP and immunoblotting detection showed the interaction between NBR1 and CKAP4. **g** Co-IP and immunoblotting detection showed the binding of P62 with CKAP4 and NBR1. **h** siNBR1 increased P62 and decreased LC3B II. **i** siNBR1 decreased the P62 bodies ($n = 5$ cells per group). The samples derive from the same experiment but different gels for NBR1 and ACTB, another for P62 and LC3B were processed in parallel. **j**–**l** Representative immunofluorescence images (**j**) and quantification (**k**, **l**, $n = 15$ cells per group) showing siCKAP4 inhibited the co-localization of NBR1 with P62 bodies. The ratio quantified by comparing the number of NBR1-positive P62 bodies to all P62 bodies per cell. Scale bar: 10 μm. **m** A schematic diagram illustrating the mechanisms of *P. micra* TmpC promoted OSCC metastasis, created in figdraw.com. Data were shown as mean ± SD. Blots are representative of at least two biological replicate experiments with similar results (**b**–**h**). One-way ANOVA with Turkey's test was used to examine the statistical significance between groups.

incubation, the invaded or migrated cells were fixed and stained. Random images were taken under a light microscope, and three independent replicates were analyzed for consistency.

Wound healing assay

The back of each 6-well plate was marked for a uniform position before the experiment. OSCC cells (1×10^6 per well) were grown until confluence and damaged with a pipette tip. Cells from each well were then co-incubated with *P. micra* (Indicated MOI or MOI = 100) or stimulated with TmpC (Indicated concentration or 0.1 mg/mL) simultaneously. Cell images were taken after 24 h. The wound size of each well was calculated as the distance between the edges.

Western blots

Mice fresh OSCC tumor tissues or cultured OSCC cells underwent lysis in RIPA buffer containing phosphatase and protease inhibitors. Proteins of equal mass were loaded onto an SDS-PAGE gel (EpiZyme, China) and transferred to a PVDF membrane (Millipore, Billerica, CA, USA) for blotting with specific antibodies. Among, CKAP4, E-cadherin, N-cadherin, GLUT1, HK2, et al. were purchased from ProteinTech (Wuhan, China), HIF-1α, Flag Tag, Goat anti-Rabbit IgG, and Goat anti-Rabbit IgG were purchased from Zen Bio (Chengdu, China), RanBP-2 was purchased from Santa (USA), LC3B was purchased from Cell Signaling Technology (USA). All antibodies are detailed in Supplementary Table 5. Protein bands were visualized using the Amersham Imager 680 (GE, America). Samples derive from the same experiment and that blots were processed in parallel. Images have been cropped for presentation. All uncropped images for all blots are provided as source data.

Bacteria screening from transcriptome data

The transcriptome data were downloaded from the GEO database under the accession number GSE227919. The clean sequencing data in fastq format were aligned to the reference genome GRCh38 via bowtie2 software (version 2-2.5.1). Quantitative analysis of the mapped data was performed utilizing the featurecounts method (subread 2.0.6) to obtain the mRNA expression. The unmapped data were handled with kraken2 software to align the Kraken microbes standardDB. Bracken software was then used to organize the output of kraken2. Ultimately, we got both mRNA expression and bacteria abundance in each sample.

Real-time quantitative polymerase chain reaction (RT-qPCR)

Cellular RNA was extracted using TRIzol reagent (CWBIO, Beijing, China) and converted to cDNA via the HiFiScript cDNA Synthesis kit (Vazyme). Then, qRT-PCR was conducted with UltraSYBR Mixture (CWBIO) to quantify relative mRNA levels, normalized against β-actin using the $2^{(-\Delta\Delta ct)}$ method. The primer sequences used in this process are detailed in Supplementary Table 5.

Single-cell RNA sequencing (scRNA-seq) and data analysis

Fresh OSCC tissues were retrieved from tongue orthotopic xenograft mice, and three repeats were prepared for each group. Samples were then sent to Singleron Company for subsequent scRNA-seq, and sequencing data was obtained through the pipeline of Singleron Company. Single cells were captured using the SCOPE-chip microfluidic technology, and millions of barcoding beads carrying unique cell barcodes were added to the chip micropore, ensuring that only one barcoding bead fell into each micropore. After cell lysis, barcoding beads with unique cell labels (Barcode) and molecular labels (UMI) capture mRNA by binding to the poly (A) tail on mRNA and then label the mRNA and cells. Barcoding beads were collected and mRNA was reversely transcribed into cDNA before amplification. A sequencing library suitable for the Illumina sequencing platform was constructed by steps such as fragmentation and splicing cDNA. The scRNA-seq data were first mapped with the human genome (GRCh38), and the unmapped sequences were mapped with the mouse genome (mm10).

The R package Seurat v5.0.1 was applied to analyze these data. In the quality control phase, any cell complying with one of the criteria below was removed: having more than 20% transcripts of mitochondrial genes, expressing fewer than 200 genes, or having fewer than 500 unique molecular identifiers (UMIs). The doublets were predicted and removed using the R package DoubletFinder v2.0.3. Data were integrated using R package harmony v1.2.0. The non-negative Matrix Factorization (NMF) method was used for dimensionality reduction to obtain an NMFfit object, and then the RunUMAP function was performed to cluster and the results were displayed using the DimPlot function. The function of "FindAllMarkers" in the Seurat package was used to analyze the changes in gene expression between clusters, and the highly expressed genes within the group were shown in heatmaps or volcano plots. Further functional enrichment analysis was performed on the findings of differential gene expression analysis using the clusterProfiler v4.10.0 package, and the significant enrichment pathways of each cell type were displayed using the dotplot. Moreover, the irGSEA package was selected to calculate enrichment scores under Hallmark gene sets using the AUCell method, and visualize the enrichment results of clusters using heatmap. In addition, GSVA demonstrated differences between the experimental group and the control group based on the hallmark and KEGG pathways. To characterize the tissue distribution of meta clusters (cell type), odds ratio (OR) values were calculated to evaluate the tissue preference of single cells. Intercellular communication network analysis was performed using CellChat v1.6.1 and differences in cell communication between the experimental group and the control group were compared.

RNA sequencing and analysis

Total RNA was extracted from CAL27 cells stimulated by *P. micra* (MOI = 100) or PBS, and three repeats were prepared for each group. Then, samples were sent to Novogene Tech for subsequent sequencing. Quality control was performed on raw data using fastp (0.23.4). The clean data obtained through quality control were aligned to the reference genome GRCh38 via bowtie2 (2-2.5.1). Quantitative analysis was performed using feature Counts (subread 2.0.6) to obtain the expression profile for each sample. Differential analysis was performed using the limma (version 3.58.1) method. The differentially expressed genes were screened by p value < 0.01 and foldchange > 1.5, and

https://doi.org/10.1038/s41467-025-57530-1

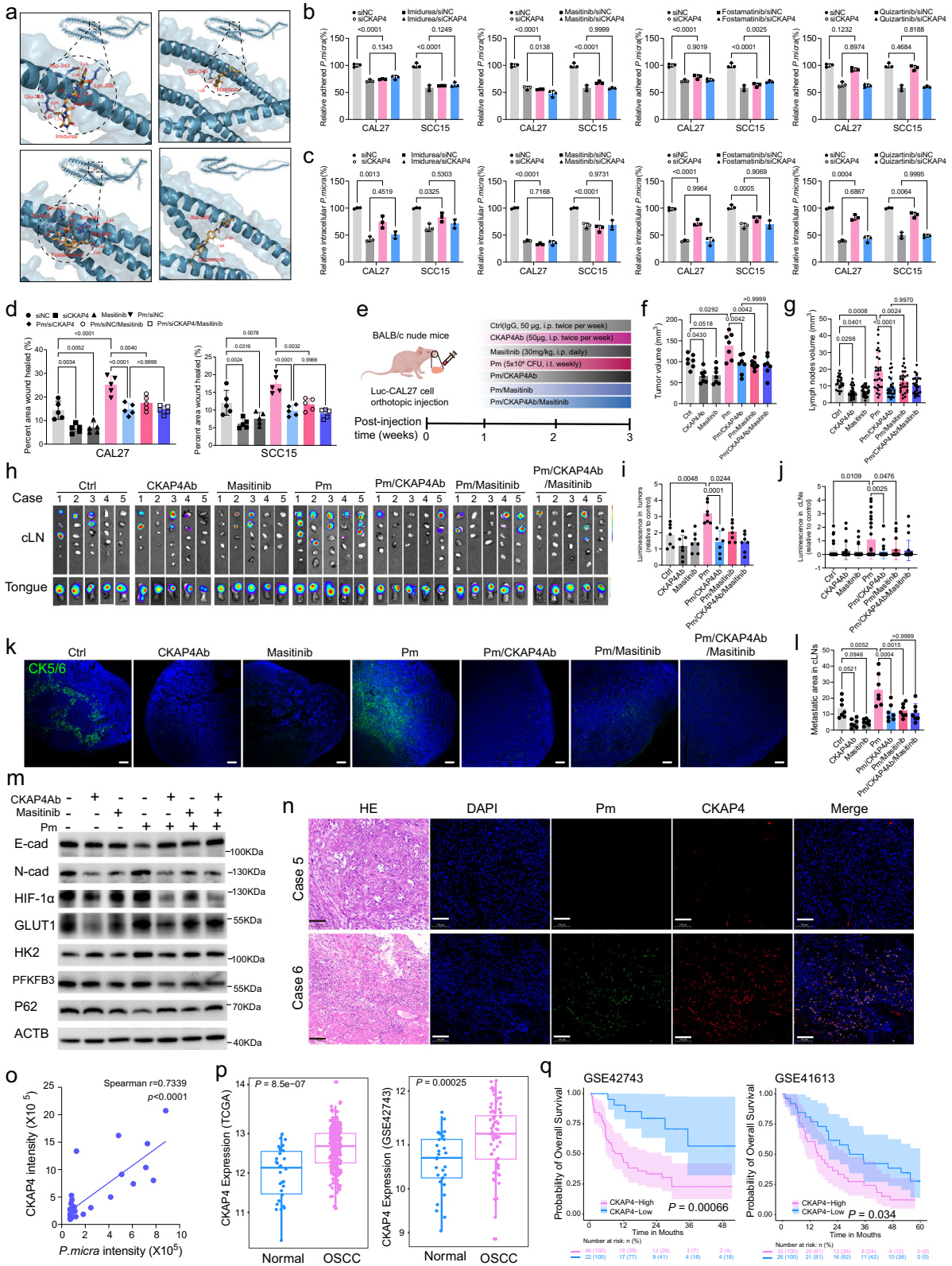

plotted in the volcano and heatmap. Enrichment of GO and KEGG pathways was implemented using filtered differentially expressed genes, and significant results were shown in bubble plots with $p < 0.05$. On the other hand, GSEA analysis was performed using all gene sets to compare the pathway changes between the experimental group and the control group. The significant result ($p < 0.05$) was shown using GseaVis package (version 0.0.5).

Immunofluorescence (IF)

OSCC cells were fixed with 4% paraformaldehyde for 20 min after they were seeded on chamber slides. The slides were incubated with 0.2% TritonX-100 (Beyotime, China) for 15 min and blocked with 3% BSA for 30 min. After three times washing by PBS, cells were incubated with primary antibodies in a wet chamber overnight at 4°C. The next day, the slides were washed by PBST three times and incubated with

Fig. 7 | Blockade of CKAP4 attenuated *P. micra*/TmpC-promoted OSCC metastasis. a Plausible binding mode of CKAP4 with imidurea, masitinib, fostamatinib, and quizartinib. **b** and **c** The impact of imidurea, masitinib, fostamatinib, and quizartinib on *P. micra* attachment (**b**) and invasion (**c**) to the OSCC cells ($n = 3$ biological replicates per group). **d** Wound-healing migration assays showed the impact of masitinib on *P. micra*-promoted OSCC motility. The average rate quantified in five randomly selected fields. Scale bar: 100 μm. **e** Schematic diagram showing OSCC orthotopic xenograft therapy model. **f** and **g** Quantification of tumor volume (**f**) and cLNs volume (**g**) from 7 mice per group. **h** Representative luciferase images of tongue and cLNs. **i** and (**j**) Quantification of bioluminescence in tumor (**i**) and cLNs (**j**) from 5 mice per group. **k** Representative immunofluorescence images of CK5/6 in cLNs. Scale bar: 100 μm. **l** Quantification of metastatic area in cLNs ($n = 7$ mice per group). **m** Western blot of E-cadherin, N-cadherin, HIF-1α, HK2, PFKFB3 and P62 in OSCC orthotopic xenograft model (mixed 3 mice per group, blots are representative of at least two biological replicate experiments with similar results. The samples derive from the same experiment but different gels for N-cadherin and GLUT1, another for HK2 and ACTB, another for HIF-1α and PFKFB3, another for E-cadherin and P62 were processed in parallel). **n** and **o** Representative images (**n**) and Spearman correlation (**o**) of *P. micra* abundance and CKAP4 expression in OSCC tissue. Scale bar: 100 μm. **p** The expression of CKAP4 in TCGA-HNSCC (Normal, $n = 30$ independent samples; OSCC, $n = 262$ independent samples) and GEO GSE42743 dataset (Normal, $n = 29$ independent samples; OSCC, $n = 74$ independent samples). The lower and upper hinges of the box represent the 25th and 75th percentiles, and the whiskers extend to the minimum and maximum values within 1.5 times the interquartile range. The median value is depicted by the line within the box. **q** Kaplan-Meier survival analysis and the log-rank test of overall survival rate in GEO GSE42743 and GSE41613 dataset. Data were shown as mean ± SD. One-way ANOVA with Turkey's test (**b**, **c**, **d**, **f**, **g**, **i**, **j**, **l**), two-sided spearman test (**o**) and two-sided Wilcox test (**p**) were used to examine the statistical significance between groups.

secondary antibodies for 1 h at room temperature. These cells were then stained with DAPI.

For detection of *P. micra* and CKAP4 colocalization, *P. micra* was labeled with CFSE (20 μM) for 0.5 h before co-culture with OSCC cells for another 2 h. Cells were fixed with 4% paraformaldehyde for 15 min and incubated with the anti-CKAP4 antibody (1: 100 dilution) at 4 °C overnight. After washing with PBS, secondary antibody incubation was performed at room temperature for 1 h using Alexa Fluor 594-conjugated goat anti-rabbit IgG (1:500 dilution). Images were acquired using a confocal microscope.

Autophagic flux detection

CAL27 and SCC15 cells were infected with mRFP-GFP-LC3 adenoviruses following the manufacturer's protocol. After adenoviruses infection 24 h, the cells were stimulated with *P. micra* for another 24 h or transfected with siRNA 24 h prior to infection and then fixed with 4% paraformaldehyde for 30 min. Nuclei were re-stained with DAPI for 5 min. All procedures were performed in the dark at RT. Finally, a confocal laser scanning microscope was used to image the cells in confocal dishes. The autophagic flux is enhanced when there is an increase in both yellow and red dots within cells. Conversely, the autophagic flux is deemed to be obstructed, if only the yellow dot signal rises without a change in the red dot signal, or if both yellow and red dots decrease.

In vitro gene silencing

OSCC cells were seeded in 24 or 6-well plates and incubated in a culture medium with 10% FBS overnight. Thereafter, the medium was replaced with a fresh medium and siRNAs were transfected into cells via Lipofectamine 3000 transfection reagents (Invitrogen, Carlsbad, California, USA) in opti-MEM (Genom, China). The following sequences of siRNAs are listed in Supplementary Table 5.

Lactate production assay and glucose uptake assay

The L-Lactate Assay Kit (Elabscience, China) was used to accurately measure lactate production. Similarly, the Glucose Uptake Colorimetric Assay Kit (Elabscience, China) facilitated the assessment of glucose uptake, following the recommended protocols. In the lactate assay, the cells were seeded in 6-well culture plates and incubated for 24 h at 37 °C. After a starvation period of 2 h, the supernatants of each group were gathered and underwent deproteinization. The subsequent measurement of lactate production was conducted using a microplate reader at 450 nm.

Regarding the glucose uptake assay, the cells underwent specific treatments to assess their glucose uptake capabilities. The levels of glucose uptake were quantitatively determined by measuring the optical density (OD) in a microplate reader at 412 nm. All experiments were conducted in triplicate to ensure reproducibility and reliability of the results.

Rescue experiments

The pLenti-U6-CKAP4-shRNA-CMV-copGFP-P2A-puro vector was designed and constructed by WZ Biosciences Inc. (Shandong, China). OSCC cells were transfected with vectors using Lipo 3000. The empty vector was used as a control. 72 h post-transfection, puromycin (10 μg/mL) was added to the cells in a 6-well plate. Fresh medium containing puromycin was replaced every 2 days for a continuous selection period of 14 days, until the proportion of fluorescent cells observed under a microscope reached 100%. Western blot was used to verify the knockout of CKAP4 in CAL27 and SCC15 cells. The wild-type CKAP4 and CKAP4 mutant lacking the TmpC-binding site (Δ991-1350) were synthesized and cloned into pENTER vectors by WZ Biosciences Inc. These vectors were transfected into CKAP4 knockdown cells used Lipo 3000. After transfection 48 h, cells were stimulated with *P. micra* for 24 h, Then, cells were used for western blot, migration and invasion assay. The expression of CKAP ^{WT} and CKAP4 $^{\Delta 991\text{-}1350}$ were verified by Flag expression.

Construction of *P. micra* ΔtmpC

The gene knockout of tmpC is based on the natural competence of *P. micra*. Targeted mutagenesis against ATCC33270 was designed using cloning-independent methodologies.[55,56] Initially, a gene knockout construct was built, utilizing ermB as the resistance selection marker, which was synthesized by BGI. The ermB gene was flanked by approximately 1 kb of upstream and downstream homologous sequences of tmpC. During the knockout process, approximately 1 ug DNA fragment was first added dropwise onto a BHI plate and allowed to be fully absorbed under anaerobic conditions. Subsequently, bacterial suspension in the logarithmic growth phase (OD = 0.4) was overlaid onto the fully absorbed DNA fragment and incubated for 1–2 days. The bacteria were then harvested and plated onto BHI plates containing erythromycin for anaerobic cultivation for 5–7 days. Transformants were screened using primers 1 F/2 R.

Recombinant protein production and purification

The full TmpC gene of *P. micra* and the CKAP4 gene of Homo sapiens were synthesized by Sangon Biotech (Shanghai, China). After rigorous verification, the prokaryotic expression vector was successfully transformed into *E. coli* BL21(DE3) strains. These E. coli cells were cultivated in LB medium until they reached an OD600 value of 0.6, indicating optimal growth conditions. Subsequently, isopropyl β-d-1-thiogalactopyranoside (IPTG) at 0.5 mmol·L-1, sourced from Aladdin in Shanghai, China, was used to induce the cultures for 2.5 h.

A His-tag Protein Purification Kit (Byotime, Shanghai, China) was employed for TmpC purification and a GST-tag Protein Purification Kit was applied for CKAP4 purification. Furthermore, Amicon® Ultra-15 Centrifugal Filters from Millipore were used to efficiently desalt, diafilter, and concentrate the purified protein, ensuring its purity and concentration for further experiments.

Agarose gel electrophoresis
To fully dissolve the agarose, combine 0.8 grams of agarose with 80 milliliters of 1 × TAE buffer solution and heat the mixture in a microwave. Before adding 8 microliters of Solargel Red, vigorously stir the mixture. Once the mixture reaches approximately 50 °C, pour it into the tank and allow it to cool fully. Ensure the agarose gel is entirely submerged in the TAE buffer by positioning it in the electrophoresis tank. Load the sample holes with DNA samples, and then adjust the voltage to 100 volts for a duration of 30 minutes. Capture images using the UV imaging system.

Blockade of CKAP4 with neutralizing antibodies
For CKAP4 blockade in vitro, OSCC cells were pre-incubated with anti-CKAP4 antibodies (Santa, catalog number sc-393544; dilution ratio, 1:100) or isotype control (Santa, catalog number sc-2025; dilution ratio, 1:50) for 2 h before the addition of *P. micra* or *P. micra*Δ*tmpC*.

His pull-down assay
The Pierce pull-down polyhis protein: protein interaction kit (Thermo Fisher Scientific, MA, USA) was used for His pull-down analysis. After the isolation of pull-down proteins, they underwent proteolytic digestion to yield peptides, which were subsequently identified by Liquid Chromatography-Mass Spectrometry (LC-MS), also provided by Thermo Fisher Scientific. This approach can accurately determine the interacting proteins.

Immunoprecipitation (IP) assay
To investigate the interaction between TmpC and CKAP4, OSCC cells were first pre-incubated with 0.1 mg/ml of TmpC for 120 min. Subsequently, the cells were incubated at 4 °C overnight with either an IgG from Santa Cruz Biotechnology (Texas, USA) or anti-His antibody from Proteintech. Then, protein A/G agarose beads from Santa Cruz Biotechnology were employed to isolate and capture the resulting protein complexes. After thorough washing, the antibody-bound complexes were eluted and Western blot analysis was performed as previously described, allowing for a detailed examination of the TmpC-CKAP4 interaction.

Co-immunoprecipitation (Co-IP) assay
Cells stimulated with *P. micra*/TmpC were lysed at 4 °C for 30 min with a complete protease inhibitor cocktail and phosphatase inhibitor as well as 1% NP-40 lysis buffer (Beyotime, P0013F). Centrifugation was conducted to discard lysates. The supernatant at 100 µl was used as an input and the left was incubated with anti-CKAP4 (Proteintech, 16686-1-AP), anti-NBR1(Santa, sc-130380), anti-RanBP2 (Santa, sc-74518) or ant-P62 (Proteintech, 18420-1-AP). The mouse or rabbit IgG was added to the supernatant and incubated overnight at 4 °C. Protein A/G-magnetic beads (Santa, sc-2003) were incubated at 4 °C for 2 h and boiled for 10 min with loading buffer, and the complex was washed with 1% NP-40 lysis buffer three times.

Surface plasmon resonance (SPR) analysis
SPR analysis was conducted using a Biacore T200 (GE Healthcare, MA, USA). Amine coupling chemistry was used to immobilize about 200 RU of His-tagged recombinant TmpC on a sensor chip CM5. Unreacted moieties were blocked with ethanolamine. Recombinantly purified CKAP4 went through a sensor chip at various concentrations. None coated flow cell was used as a nonspecific binding control. Data was analyzed using Biacore T200 software.

Multiple sequences alignment analysis
The amino acid sequence of spike protein of SARS-CoV-2 (P0DTC2) was downloaded from the NCBI website (https://www.ncbi.nlm.nih.gov/). Stereochemistry structure of SARS-CoV-2 spike protein was searched in the PDB database and obtained with entry ID 7ek6 (https://www.rcsb.org/). Multiple sequences alignment analysis was performed by the mafft software[57] using the default parameters and visualized by the ESPript[58].

Docking-based interaction
The amino acid sequences of protein TmpC and CKAP4 were obtained from the UniProt website. Sequences of two proteins were then uploaded to the alphafold server (AlphaFold 3, https://alphafoldserver.com/) to do the protein-protein docking analysis. After the docking forecast, molecular conformation with lowest energy was selected and Pymol software was utilized to further analyze and visualize the.cif files of alphafold server.

Docking-based virtual screening
From the DrugBank database (Release Version 5.1.12), we downloaded the structures of 9468 drug molecules in sdf format. Utilizing the Openbabel software, we segmented the dataset and then converted the molecules in batches into the mol2 format. The amino acid sequence of the protein CKAP4 was downloaded from UniProt. Then, the sequence was uploaded to the alphafold server (https://alphafoldserver.com/) to obtain an optimal structure of CKAP4. To improve the reliability of the predicted structure, a sequence fragment with very low pIDDT score was removed by the Pymol software. The LeDock software[59] was then used to conduct a batch virtual screening to dock small molecules (mol2 format) and CKAP4. Ultimately, results with low energy scores (kcal/mol) were selected for further experimental verification.

Bacterial attachment and invasion assay
OSCC cells were cultured with *P. micra* (MOI = 100) in a 6-well plate for 2 h in antibiotic-free DMEM or DMEM/F-12 medium supplemented with 10% FBS under anaerobic conditions. For the invasion assay and bacterial attachment, the cells were thoroughly washed with warm PBS three times, followed by lysis with 1% TritonX-100 for 5 min. The resulting cell lysate was then gathered and plated on Schaedler agar for an enumeration of attached bacterial counts through serial dilution. For the invasion assay, OSCC cells were treated with ampicillin and gentamicin (100 µg/mL) for another 2 h before enumerating bacterial colony-forming units (CFU). For flow cytometry analysis, *P. micra* was treated by CFSE (20 µM) for 0.5 h before co-culture with OSCC cells for another 2 h. Antibiotic-treated or non-treated cells were collected and subjected to flow cytometric analysis.

Scanning electron microscopy (SEM)
OSCC cells were seeded in sterile coverslips and co-cultured with *P. micra* (MOI = 100) for 2 h. Subsequently, the cells were then washed thoroughly three times with freshly prepared Sorensen's phosphate buffer (0.1 M, pH 7.2), followed by fixation overnight using 2.5% glutaraldehyde fixative. The fixed coverslips were then washed three more times with Sorensen's phosphate buffer and further fixed using 1% osmium tetroxide for a duration of 2 hours. The specimens were then rinsed with distilled water, dehydrated, and coated with gold palladium. Finally, the prepared specimens were measured under a Cold Field Scanning Electron Microscope (Hitachi SU8010).

Transmission electron microscopy (TEM)
OSCC cells were co-cultured with *P. micra* (MOI = 100) for 2 h. The cells were initially pre-fixed for 2 h in 0.1 M sodium cacodylate buffer (SCB) at pH 7.2 using a 2.5% (v/v) glutaraldehyde solution. Subsequently, the cells were thoroughly washed three times with 0.2 M SCB and post-fixed at room temperature for 1 h in 1% (w/v) osmium tetroxide dissolved in 0.2 M SCB. Afterwards, the cells underwent a dehydration process through a series of graded ethanol concentrations, culminating in 100% acetone. Once dehydrated, the cells were infiltrated with a

combination of acetone-Epon 812 resin mixture, eventually transitioning to 100% Epon 812 resin. Ultra-thin serial sections were carefully gathered on a copper formvar-coated slot grid, and these sections were stained with 2% (w/v) uranyl acetate, leading citrate to enhance contrast. Finally, the sections were visualized and examined under an electron microscope.

Luciferase imaging

Mice were anaesthetized and administered with D-luciferin at the dose of 150 mg/kg body weight. After 10 min, tumor and lymph tissues were extracted and Luciferase imaging (IVIS Spectrum) was performed.

Key resources were list in Supplementary Table 5.

Statistics and reproducibility

Each experiment was performed at least two biological replicates. Statistical analysis was performed using GraphPad Prism 9.5 (GraphPad Software, Inc.). two-sided unpaired Student's t test was performed to compare the means between two groups. Multiple group comparison was conducted by o One-way analysis of variance (ANOVA) with Turkey's test. Two-sided Wilcoxon test was used to examine the abundance of *P. micra* in different groups. The survival curves were plotted using the Kaplan-Meier method and compared with the log-rank test. Details of statistical analysis were mentioned in each Figure legends. The probability values of < 0.05 were considered statistically significant. Exact *p*-value was provided.

Reporting summary

Further information on research design is available in the Nature Portfolio Reporting Summary linked to this article.

Data availability

The RNA sequencing data of CAL27 with or without *P. micra* infection and scRNA sequencing data in this study have been deposited in the Genome Sequence Archive in National Genomics Data Center, China National Center for Bioinformation/Beijing Institute of Genomics, Chinese Academy of Sciences under accession code GSA-Human: HRA007593 and HRA007594. RNA sequencing data for analyzing the abundance of intertumoral *P. micra* was retrieved form Gene Expression Omnibus (GEO) under accession GSE227919. Microbiome data was retrieved form Sequence Read Archive under accession PRJNA866676. RNA sequencing data for analyzing the correlation between CKAP4 and the survival rate of OSCC patients was retrieved form GEO under accession GSE42743 and GSE41613 [https://www.ncbi.nlm.nih.gov/geo/query/acc.cgi]. Mass spectrometry raw data have been deposited to the ProteomeXchange Consortium via the iProX partner repository with the dataset identifier PXD054166 [https://proteomecentral.proteomexchange.org]. Source data are provided as a Source Data file. Source data are provided with this paper.

References

1. Vadovics, M. et al. Candida albicans enhances the progression of oral squamous cell carcinoma in vitro and in vivo. *mBio* **13**, e0314421 (2021).
2. Tang, Q. et al. Circadian clock gene Bmal1 inhibits tumorigenesis and increases paclitaxel sensitivity in tongue squamous cell carcinoma. *Cancer Res.* **77**, 532–544 (2017).
3. Chinn, S. B. & Myers, J. N. Oral cavity carcinoma: current management, controversies, and future directions. *J. Clin. Oncol.: Off. J. Am. Soc. Clin. Oncol.* **33**, 3269–3276 (2015).
4. J, S. H. & Hysi, D. Methods and risk of bias in molecular marker prognosis studies in oral squamous cell carcinoma. *Oral. Dis.* **24**, 115–119 (2018).
5. Buchta Rosean, C. et al. Preexisting commensal dysbiosis is a host-intrinsic regulator of tissue inflammation and tumor cell dissemination in hormone receptor-positive breast cancer. *Cancer Res.* **79**, 3662–3675 (2019).
6. Riquelme, E. et al. Tumor microbiome diversity and composition influence pancreatic cancer outcomes. *Cell* **178**, 795–806.e712 (2019).
7. Yu, T. et al. Fusobacterium nucleatum promotes chemoresistance to colorectal cancer by modulating autophagy. *Cell* **170**, 548–563.e516 (2017).
8. Fu, A. et al. Tumor-resident intracellular microbiota promotes metastatic colonization in breast cancer. *Cell* **185**, 1356–1372.e1326 (2022).
9. Kong, C. et al. Fusobacterium nucleatum promotes the development of colorectal cancer by activating a cytochrome P450/epoxyoctadecenoic acid axis via TLR4/keap1/NRF2 signaling. *Cancer Res.* **81**, 4485–4498 (2021).
10. Lu, X. et al. Long non-coding RNA EVADR induced by Fusobacterium nucleatum infection promotes colorectal cancer metastasis. *Cell Rep.* **40**, 111127 (2022).
11. Saikia, P. J., Pathak, L., Mitra, S. & Das, B. The emerging role of oral microbiota in oral cancer initiation, progression and stemness. *Front. Immunol.* **14**, 1198269 (2023).
12. Guo, Z. C. et al. *Porphyromonas Gingivalis Promotes The Progression Of Oral Squamous Cell Carcinoma By Stimulating The Release Of Neutrophil Extracellular Traps In The Tumor Immune Microenvironment. Inflammation research: official journal of the European Histamine Research Society* (2023).
13. Ren, J. et al. P. gingivalis infection upregulates PD-L1 expression on dendritic cells, suppresses CD8+ T-cell responses, and aggravates oral cancer. *Cancer Immunol. Res.* **11**, 290–305 (2023).
14. Chen, G. et al. Fusobacterium nucleatum outer membrane vesicles activate autophagy to promote oral cancer metastasis. *J. Adv. Res.* **56**, 167–179 (2024).
15. Sun, J. et al. F. nucleatum facilitates oral squamous cell carcinoma progression via GLUT1-driven lactate production. *EBioMedicine* **88**, 104444 (2023).
16. Sillanpää, J., Nallapareddy, S. R., Singh, K. V., Ferraro, M. J. & Murray, B. E. Adherence characteristics of endocarditis-derived Streptococcus gallolyticus ssp. gallolyticus (Streptococcus bovis biotype I) isolates to host extracellular matrix proteins. *FEMS Microbiol. Lett.* **289**, 104–109 (2008).
17. Koeth, L. M. et al. Surveillance of susceptibility patterns in 1297 European and US anaerobic and capnophilic isolates to co-amoxiclav and five other antimicrobial agents. *J. antimicrobial Chemother.* **53**, 1039–1044 (2004).
18. Chang, Y. et al. Parvimonas micra activates the Ras/ERK/c-Fos pathway by upregulating miR-218-5p to promote colorectal cancer progression. *J. Exp. Clin. cancer Res.: CR* **42**, 13 (2023).
19. Zhao, L. et al. Parvimonas micra promotes colorectal tumorigenesis and is associated with prognosis of colorectal cancer patients. *Oncogene* **41**, 4200–4210 (2022).
20. Coker, O. O. et al. Mucosal microbiome dysbiosis in gastric carcinogenesis. *Gut* **67**, 1024–1032 (2018).
21. Nie, F. et al. Characteristics of microbial distribution in different oral niches of oral squamous cell carcinoma. *Front. Cell. Infect. Microbiol.* **12**, 905653 (2022).
22. Khan, M. M. et al. Total RNA sequencing reveals gene expression and microbial alterations shared by oral pre-malignant lesions and cancer. *Hum. genomics* **17**, 72 (2023).
23. Yu, X. et al. Molecular mechanisms of TWIST1-regulated transcription in EMT and cancer metastasis. *EMBO Rep.* **24**, e56902 (2023).
24. Li, B. et al. LncRNA GAL promotes colorectal cancer liver metastasis through stabilizing GLUT1. *Oncogene* **41**, 1882–1894 (2022).
25. Liu, J. et al. Metabolic enzyme LDHA activates Rac1 GTPase as a noncanonical mechanism to promote cancer. *Nat. Metab.* **4**, 1830–1846 (2022).

26. Jing, X. et al. Role of hypoxia in cancer therapy by regulating the tumor microenvironment. *Mol. cancer* **18**, 157 (2019).
27. Yang, Z. et al. HIF-1α drives resistance to ferroptosis in solid tumors by promoting lactate production and activating SLC1A1. *Cell Rep.* **42**, 112945 (2023).
28. Lu, X. et al. UBE2M-mediated neddylation of TRIM21 regulates obesity-induced inflammation and metabolic disorders. *Cell Metab.* **35**, 1390–1405.e1398 (2023).
29. Li, Q. et al. HIF-1α-induced expression of m6A reader YTHDF1 drives hypoxia-induced autophagy and malignancy of hepatocellular carcinoma by promoting ATG2A and ATG14 translation. *Signal Transduct. Target. Ther.* **6**, 76 (2021).
30. Tan, V. P. & Miyamoto, S. HK2/hexokinase-II integrates glycolysis and autophagy to confer cellular protection. *Autophagy* **11**, 963–964 (2015).
31. Li, W. et al. Tumor-derived lactate promotes resistance to bevacizumab treatment by facilitating autophagy enhancer protein RUBCNL expression through histone H3 lysine 18 lactylation (H3K18la) in colorectal cancer. *Autophagy* **20**, 114–130 (2024).
32. Ritterhoff, T. et al. The RanBP2/RanGAP1*SUMO1/Ubc9 SUMO E3 ligase is a disassembly machine for Crm1-dependent nuclear export complexes. *Nat. Commun.* **7**, 11482 (2016).
33. Lin, Y., Wang, M., Xiao, Z. & Jiang, Z. Hypoxia activates SUMO-1-HIF-1α signaling pathway to upregulate pro-inflammatory cytokines and permeability in human tonsil epithelial cells. *Life Sci.* **276**, 119432 (2021).
34. Guo, Q. et al. Glioblastoma upregulates SUMOylation of hnRNP A2/B1 to eliminate the tumor suppressor miR-204-3p, accelerating angiogenesis under hypoxia. *Cell death Dis.* **14**, 147 (2023).
35. Kurusu, R. et al. Integrated proteomics identifies p62-dependent selective autophagy of the supramolecular vault complex. *Developmental cell* **58**, 1189–1205.e1111 (2023).
36. Lohavanichbutr, P. et al. A 13-gene signature prognostic of HPV-negative OSCC: discovery and external validation. *Clin. Cancer Res.: Off. J. Am. Assoc. Cancer Res.* **19**, 1197–1203 (2013).
37. Zhao, Y. et al. Comprehensive analysis of tumor immune microenvironment characteristics for the prognostic prediction and immunotherapy of oral squamous cell carcinoma. *Front. Genet.* **13**, 788580 (2022).
38. Stasiewicz, M. & Karpiński, T. M. The oral microbiota and its role in carcinogenesis. *Semin. Cancer Biol.* **86**, 633–642 (2022).
39. Conde-Pérez, K. et al. Parvimonas micra can translocate from the subgingival sulcus of the human oral cavity to colorectal adenocarcinoma. *Mol. Oncol.* https://doi.org/10.1002/1878-0261.13506 (2023).
40. Battaglia, T. W. et al. A pan-cancer analysis of the microbiome in metastatic cancer. *Cell* **187**, 2324–2335.e2319 (2024).
41. Abdullah, M. R. et al. Crystal structure and pathophysiological role of the pneumococcal nucleoside-binding protein PnrA. *J. Mol. Biol.* **433**, 166723 (2021).
42. Fu, K. et al. Streptococcus anginosus promotes gastric inflammation, atrophy, and tumorigenesis in mice. *Cell* **187**, 882–896.e817 (2024).
43. Schweizer, A., Ericsson, M., Bächi, T., Griffiths, G. & Hauri, H. P. Characterization of a novel 63 kDa membrane protein. Implications for the organization of the ER-to-Golgi pathway. *J. cell Sci.* **104**, 671–683 (1993).
44. Kimura, H. et al. CKAP4 is a Dickkopf1 receptor and is involved in tumor progression. *J. Clin. Investig.* **126**, 2689–2705 (2016).
45. Li, K. et al. SARS-CoV-2 Spike protein promotes vWF secretion and thrombosis via endothelial cytoskeleton-associated protein 4 (CKAP4). *Signal Transduct. Target. Ther.* **7**, 332 (2022).
46. Rasmussen, N. L., Kournoutis, A., Lamark, T. & Johansen, T. NBR1: The archetypal selective autophagy receptor. *J.Cell Biol.* **221**, e202208092 (2022).
47. Deplanque, G. et al. A randomized, placebo-controlled phase III trial of masitinib plus gemcitabine in the treatment of advanced pancreatic cancer. *Ann. Oncol.: Off. J. Eur. Soc. Med. Oncol.* **26**, 1194–1200 (2015).
48. Kimura, H. et al. CKAP4, a DKK1 receptor, is a biomarker in exosomes derived from pancreatic cancer and a molecular target for therapy. *Clin. Cancer Res.: Off. J. Am. Assoc. Cancer Res.* **25**, 1936–1947 (2019).
49. Kajiwara, C. et al. p63-dependent dickkopf3 expression promotes esophageal cancer cell proliferation via CKAP4. *Cancer Res.* **78**, 6107–6120 (2018).
50. Bhavanasi, D., Speer, K. F. & Klein, P. S. CKAP4 is identified as a receptor for Dickkopf in cancer cells. *J. Clin. Investig.* **126**, 2419–2421 (2016).
51. Song, J. W. et al. GOLPH3/CKAP4 promotes metastasis and tumorigenicity by enhancing the secretion of exosomal WNT3A in non-small-cell lung cancer. *Cell death Dis.* **12**, 976 (2021).
52. Lee, K. B. et al. p63-Mediated activation of the β-catenin/c-Myc signaling pathway stimulates esophageal squamous carcinoma cell invasion and metastasis. *Cancer Lett.* **353**, 124–132 (2014).
53. Li, S. X. et al. CKAP4 inhibited growth and metastasis of hepatocellular carcinoma through regulating EGFR signaling. *Tumour Biol.: J. Int. Soc. Oncodev. Biol. Med.* **35**, 7999–8005 (2014).
54. Zhang, C. et al. Androgen deprivation therapy exacerbates Alzheimer's-associated cognitive decline via increased brain immune cell infiltration. *Sci. Adv.* **10**, eadn8709 (2024).
55. Higashi, D. L. et al. Employing cloning-independent mutagenesis of *Parvimonas micra* for the study of cell wall biogenesis. *Methods Mol. Biol.* **2727**, 57–67 (2024)
56. Higashi, D. L. et al. Development of the first tractable genetic system for *Parvimonas micra*, a ubiquitous pathobiont in human dysbiotic disease. *Microbiol. Spectr.* **10**, e0046522 (2022)
57. Katoh, K. & Standley, D. M. MAFFT multiple sequence alignment software version 7: improvements in performance and usability. *Mol. Biol. evolution* **30**, 772–780 (2013).
58. Robert, X. & Gouet, P. Deciphering key features in protein structures with the new ENDscript server. *Nucleic acids Res.* **42**, W320–W324 (2014).
59. Wang, Z. et al. Comprehensive evaluation of ten docking programs on a diverse set of protein-ligand complexes: the prediction accuracy of sampling power and scoring power. *Phys. Chem. Chem. Phys.: PCCP* **18**, 12964–12975 (2016).

Acknowledgements

We sincerely thank the foundation support of Noncommunicable Chronic Diseases-National Science and Technology Major Project (2023ZD0501400 to Q.F.) and National Natural Science Foundation of China (No. 82270980, 82071122 and 22106178 to Q.F.), the National Young Scientist Support Foundation (2019), Excellent Young Scientist Foundation of Shandong Province (No. ZR2021JQ29 to Q.F.), Taishan Young Scientist Project of Shandong Province (2019) to Q.F., Periodontitis innovation team of Jinan City (2021GXRC021 to Q.F.), Major Innovation Projects in Shandong Province (No. 2021SFGC0502 to Q.F.), Oral Microbiome Innovation Team of Shandong Province (No. 2020KJK001 to Q.F.), Shandong Province Key Research and Development Program (No. 2021ZDSYS18 to Q.F.), Project funded by China Postdoctoral Science Foundation (No. 2022M721936 to H.Q.). The authors thank Pro. Zhiquan Huang (Sun Yat-Sen University) for the gift of Luc-CAL27 cell line.

Author contributions

H.Q. performed experiments and drafted the manuscript. H.G. performed mouse experiments and bacterial culture and assisted with data statistics. M.L., T.S., M.Z., D.F. and Y.D. performed bioinformatic analyzes. X.G. performed plasmid construction, recombinant protein generation, and construction of *P. micraΔtmpC*. L.W. performed FISH and

assisted on mouse experiments. Y. L. and Z.W. assisted in cellular experiments. Z.L. assisted in mouse experiments. Q.F. designed and supervised the study and revised the manuscript. All authors approved the final version of the manuscript.

Competing interests
The authors declare no competing interests.

Additional information
Supplementary information The online version contains supplementary material available at https://doi.org/10.1038/s41467-025-57530-1.

Correspondence and requests for materials should be addressed to Qiang Feng.

Peer review information *Nature Communications* thanks Akira Kikuchi, and the other, anonymous, reviewer(s) for their contribution to the peer review of this work. A peer review file is available.